Topography, exhumation pathway, age uncertainties, and the interpretation of thermochronometer data

Katharine W. Huntington,[1] Todd A. Ehlers,[2] Kip V. Hodges,[3] and David M. Whipp Jr.[2]

Received 17 January 2007; revised 8 May 2007; accepted 31 May 2007; published 16 August 2007.

[1] The relationship between thermochronometer age and structural elevation is commonly used to infer long-term exhumation histories. Previous studies suggest that inferred exhumation rates from the conventional (one-dimensional, 1-D) age-elevation approach are sensitive to topography and variations in exhumation rate and pathway. Here we evaluate the magnitude of these effects by (1) using a 3-D thermal-kinematic model of the central Nepalese Himalaya to predict age-elevation profiles for multiple thermochronometers as a function of exhumation rate and pathway (vertical, oblique, or thrust fault), and (2) calculating the probability that the true exhumation rate will be recovered from an age-elevation profile for sample uncertainties of different magnitudes. Results suggest that profiles oriented orthogonal to long-wavelength topography and the direction of lateral transport are relatively insensitive to their influence. For profiles oriented parallel to the transport direction, horizontal transport during exhumation partly counteracts topographic effects. The difference between model imposed and 1-D exhumation rates from the slope of a best fit line through an age-elevation plot is greatest when rocks are exhumed vertically and low-temperature thermochronometers are used. The magnitude of error in 1-D exhumation rate estimates varies dramatically as a function of sample uncertainty, particularly when exhumation is rapid. The nature of this variation can be used to design sampling strategies for which 1-D interpretations of age-elevation gradients are likely to be within error of the true exhumation rate. Alternatively, if sample uncertainties can be reduced, studies that combine thermal modeling with age-elevation data can potentially provide important constraints on thermal and kinematic fields at depth. **Citation:** Huntington, K. W., T. A. Ehlers, K. V. Hodges, and D. M. Whipp Jr. (2007), Topography, exhumation pathway, age uncertainties, and the interpretation of thermochronometer data, *Tectonics*, *26*, TC4012, doi:10.1029/2007TC002108.

1. Introduction

[2] Mineral cooling histories related to rock exhumation are widely used to investigate long-term ($>\sim10^5$ years) exhumation rates. Sample cooling ages vary as a function of the subsurface thermal field and the paths and rates at which rocks travel from some effective closure isotherm to the surface. The simplest and most commonly used techniques (one-dimensional, 1-D) for interpreting exhumation rates from thermochronometer ages assume that rocks follow vertical exhumation paths, and that the closure isotherm of interest is horizontal (Figure 1a). In this approach, a sample's cooling rate can be related to the exhumation rate using an assumed geothermal gradient [e.g., *Hodges*, 2003]. Alternatively, in the "age-elevation" approach examined in this study, the relationship between sample structural elevation and cooling age can be used as a proxy for long-term exhumation rate [e.g., *Wagner and Reimer*, 1972; *Foster and Gleadow*, 1996; *Brandon et al.*, 1998; *Crowley et al.*, 2002; *Reiners et al.*, 2002; *Balestrieri et al.*, 2003; *Bartolini et al.*, 2003; *Ducea et al.*, 2003; *House et al.*, 2003; *Reiners et al.*, 2003; *Thiede et al.*, 2004] (Figure 1b).

[3] Several workers have pointed out that simple 1-D interpretations might lead to inaccurate exhumation rate estimates due to perturbations in the thermal field from topography and lateral advection from thrust faulting [*Stüwe et al.*, 1994; *Mancktelow and Grasemann*, 1997; *Stüwe and Hintermüller*, 2000; *Braun*, 2002a; *Ehlers and Farley*, 2003; *Safran*, 2003; *Braun*, 2005]. In most applications, it would be more realistic to assume that the exhumation trajectory is two- or three-dimensional and includes both lateral and vertical components [e.g., *Batt et al.*, 2001; *Ehlers et al.*, 2001; *Batt and Brandon*, 2002; *Ehlers and Farley*, 2003]. Moreover, it would be more appropriate to model the depth to the closure temperature isotherm as spatially variable due to topographic perturbations of the near-subsurface thermal field [*Stüwe et al.*, 1994; *Mancktelow and Grasemann*, 1997; *Brandon et al.*, 1998; *Stüwe and Hintermüller*, 2000; *Reiners et al.*, 2003]. Unfortunately, the practical application of more sophisticated models to infer exhumation rates [e.g., *Batt and Braun*, 1997, 1999; *Batt and Brandon*, 2002; *Bollinger et al.*, 2006; *Brewer et al.*, 2006; *Whipp et al.*, 2007] is complicated and results are often difficult to apply to other settings which may have different topography and deformation histories.

[1] Division of Geological and Planetary Sciences, California Institute of Technology, Pasadena, California, USA.
[2] Department of Geological Sciences, University of Michigan, Ann Arbor, Michigan, USA.
[3] School of Earth and Space Exploration, Arizona State University, Tempe, Arizona, USA.

0278-7407/07/2007TC002108

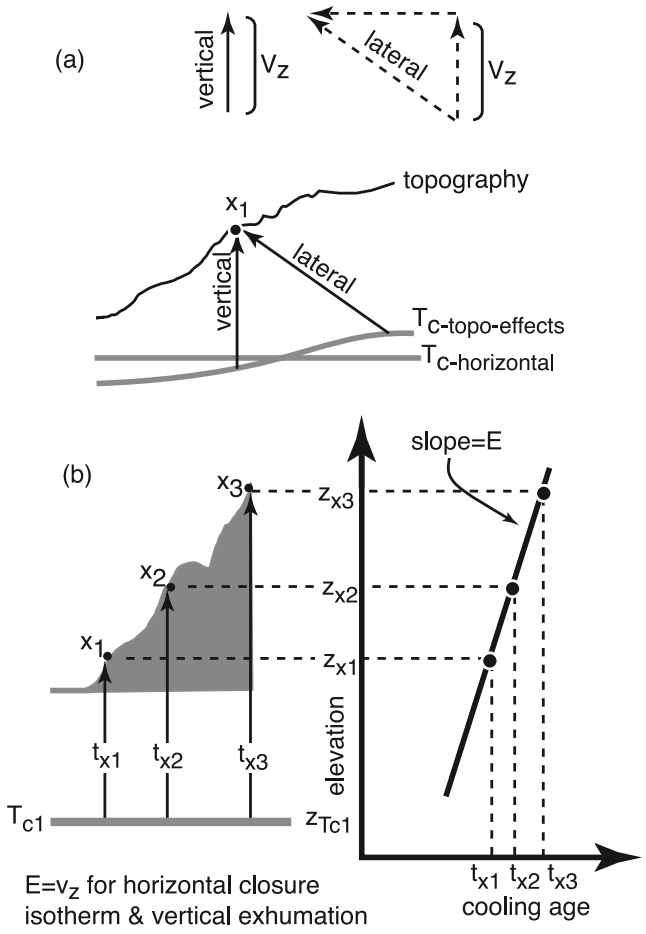

Figure 1. Terminology and age-elevation method for estimating exhumation rates from thermochronologic samples. (a) Vertical and lateral exhumation pathways for sample x_1. Pathway begins at closure isotherm, either $T_{C\text{-horizontal}}$ or $T_{C\text{-topo-effects}}$ (a damped version of the topography); v_z is the vertical velocity component of the exhumation trajectory. (b) Basic age-elevation model. Samples x_1, x_2, and x_3 are exhumed vertically from a horizontal closure isotherm at depth z_{Tc1} to points on the surface at elevations z_{x1}, z_{x2}, and z_{x3}, respectively. Cooling ages t_{x1}, t_{x2}, and t_{x3}, represent the time since samples x_1, x_2, and x_3 passed through the closure isotherm depth and are plotted versus sample elevation. The slope of the best fit line through these points (the age-elevation gradient) is defined as the apparent exhumation rate E. When the closure isotherm is horizontal and rocks are exhumed vertically, the apparent rate E is equivalent to the true exhumation rate v_z.

[4] This study builds upon previous work by quantifying general relationships and tradeoffs among thermochronometry transect orientation, topography, and rock exhumation rate and trajectory. We investigate the circumstances under which apparent exhumation rates calculated from age-elevation profiles will substantially underestimate or overestimate the vertical component of the true rate (referred to in this paper as simply "the exhumation rate" or v_z) (Figure 1a). We use a 3-D thermal model with variable exhumation rates (v_z = 0.1–3.0 mm/yr) and end-member exhumation geometries (Figures 2a–2c) to predict cooling ages for various minerals sampled at the surface (Figures 2d–2e). Furthermore, we consider the influence of sample uncertainties on interpreted exhumation rates. The probability that the true exhumation rate will be calculated from age-elevation plots is determined for different thermochronometers with variable uncertainty in measured ages.

2. Age-Elevation Transects and Apparent Exhumation Rates

2.1. One-Dimensional Interpretations

[5] The age-elevation method for estimating exhumation rates exploits the difference in elevation between samples collected in valleys and on ridges and its effect on cooling age distributions at the surface [*Wagner and Reimer*, 1972; *Wagner et al.*, 1977]. This elevation difference between samples results in shorter exhumation paths from the closure isotherm to samples collected in valleys than to samples collected from ridges. As a result, cooling age increases with sample elevation in proportion to the exhumation rate, and the age-elevation gradient is equal to the apparent exhumation rate, *E* (Figure 1b). In order for this simple model to apply, several important assumptions must be valid, including: (1) all rocks follow vertical exhumation paths from the closure isotherm to the surface, and (2) all samples pass through the closure isotherm at the same depth with respect to sea level. When these assumptions are violated, *E* may overestimate or underestimate the true exhumation rate [e.g., *Stüwe et al.*, 1994].

[6] Both topography and rock advection due to denudation and lateral transport have the potential to affect the accuracy of exhumation rate estimates from age-elevation gradients. Topography has a lateral cooling effect that compresses isotherms beneath valleys and increases the distance between isotherms under ridges, causing spatial variations in the thermal gradient. The magnitude of this effect depends on the relief and wavelength of topography as well as the exhumation rate and decays with depth [*Stüwe et al.*, 1994; *Mancktelow and Grasemann*, 1997]. Furthermore, denudation advects relatively warm rocks toward the surface, causing isotherms to shallow and thermal gradients to increase. While 2-D models have shown that age-elevation gradients may severely overestimate true exhumation rates when topographic effects are significant [e.g., *Stüwe et al.*, 1994; *Mancktelow and Grasemann*, 1997], even in the absence of topographic effects, nonvertical exhumation paths increase the distance samples must travel from the closure isotherm to the surface and can change apparent exhumation rates.

2.2. Multidimensional Considerations

[7] In addition to the complications described in section 2.1, the orientation of the sample profile with respect to the transport direction can also be important if samples are not

collected in a strictly vertical profile (i.e., on a cliff face). We illustrate some potential effects of sample profile orientation on age-elevation gradients with a thought experiment in three dimensions (X, Y, and Z), where Z is the vertical coordinate. Consider first the simplest case where the closure isotherm is horizontal (Figure 3a). This configuration might represent a high-temperature (>200°C) isotherm in a region eroding at a rate of, for example, 0.5 mm/yr. In this case if exhumation pathways are vertical, assumptions 1 and 2 from section 2.1 are satisfied and the age-elevation gradient returns an accurate exhumation rate estimate.

[8] However, when samples are transported laterally during exhumation, the 1-D model is no longer appropriate, and the age-elevation gradient may be expected to underestimate the true exhumation rate (Figure 3a). In Figure 3a,

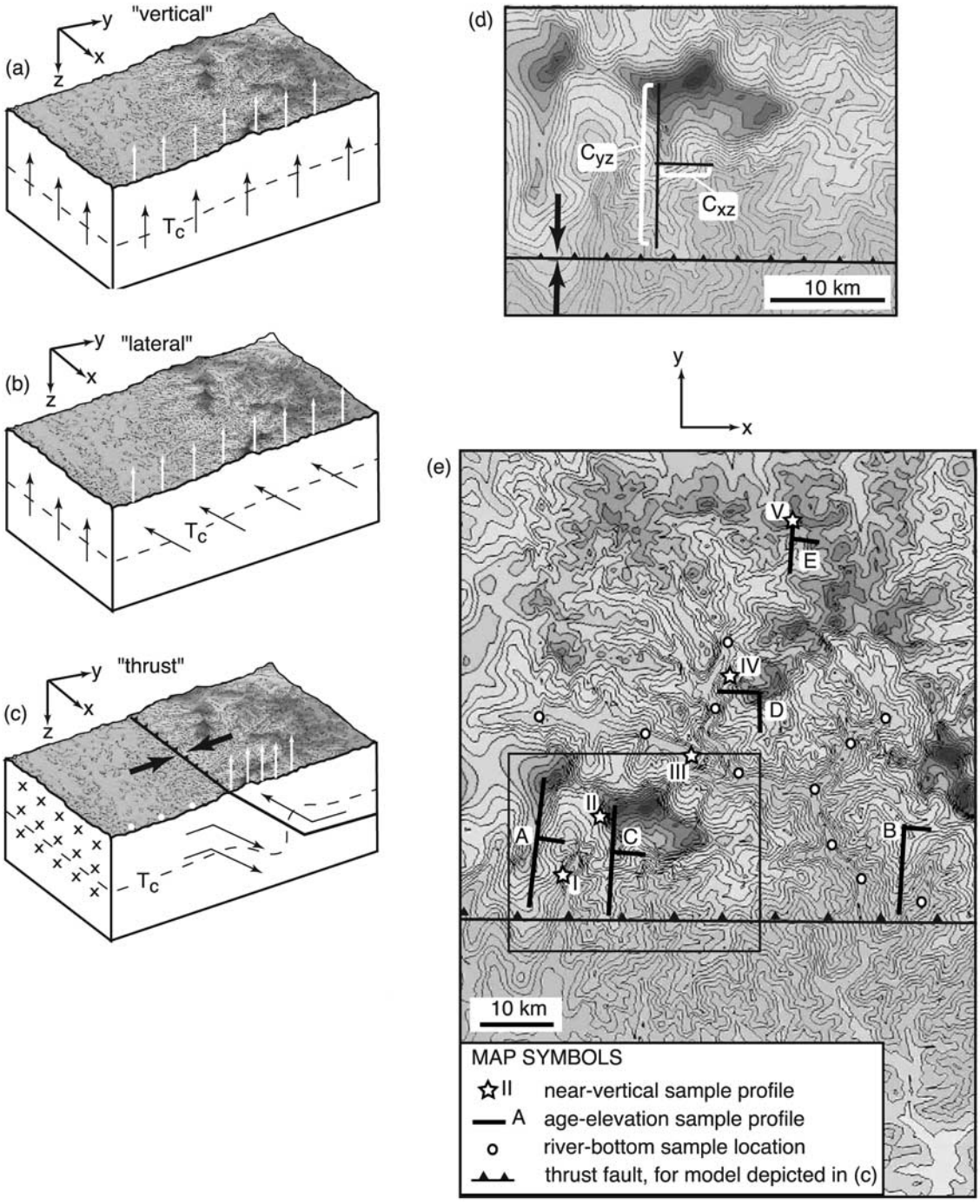

Figure 2

the sample profile and the rock trajectories are in the same plane (YZ). If the sample profile and the rock trajectories are in different vertical planes, for example if the sample profile is in plane (XZ), the magnitude of underestimation in exhumation rate is the same as in the scenario depicted in Figure 3a when the closure isotherm is flat (Figure 3b). However, the effect is different if the closure isotherm is curved in one direction due to long-wavelength (>100 km) topography [*Braun*, 2002a], as in Figures 3c–3d. In the case where the isotherm is curved in the plane of the sample profile (Figure 3c), the age-elevation calculation could overestimate the true exhumation rate when samples are transported laterally. In the case where the exhumation trajectory and the sample profile are orthogonal (Figure 3d), the apparent exhumation rate could underestimate the true exhumation rate. As summarized in Figure 3e, many different apparent exhumation rates may be expected depending on the orientation of the sample profile and exhumation trajectory.

[9] These thought experiments highlight the potential impact of topography and nonvertical exhumation pathways on sample profiles of different orientations. They also underscore the potential impact of, and need to constrain, the closure isotherm geometry when interpreting exhumation rates. Three-dimensional thermal models can provide valuable intuition regarding the magnitude of effect complex topographies can have on subsurface temperatures and age-elevation gradients [e.g., *Ehlers and Farley*, 2003; *Braun*, 2005; *Whipp et al.*, 2007].

3. The Model

3.1. Model Geometry

[10] Mountain topography varies in 3-D at many different wavelengths and amplitudes. Rather than generate a synthetic landscape for simulating subsurface thermal fields we elected to use the naturally occurring landscape of the Marsyandi drainage in the Nepal Himalaya. The Himalaya are particularly well suited for our investigation because the region is characterized by steep, high-relief (>5 km) topography and by a distribution of ridges that trend at a variety of orientations with respect to the transport direction along the Main Central Thrust (MCT) system [e.g., *Seeber and Gornitz*, 1983; *Pandey et al.*, 1995; *Bilham et al.*, 1997; *Cattin and Avouac*, 2000; *Hodges et al.*, 2004]. Furthermore, a growing number of thermochronologic studies have been conducted in this region [*Edwards*, 1995; *Brewer et al.*, 2003; *Burbank et al.*, 2003; *Blythe et al.*, 2007; *Bollinger et al.*, 2004; *Brewer et al.*, 2006; *Ruhl and Hodges*, 2005; *Huntington and Hodges*, 2006; *Huntington et al.*, 2006], and future studies will benefit from our investigations.

3.2. Coupled Thermal, Kinematic, and Age Prediction Models

[11] We used a series of coupled numerical models including a kinematic model (Figures 2a–2c), a 3-D thermal finite element model (Figure 4), and a thermochronometer age prediction model [e.g., *Ehlers and Farley*, 2003; *Whipp et al.*, 2007]. The modeling approach used is identical to that of *Whipp et al.* [2007] and *Huntington et al.* [2006], and only a brief description of the different components is presented here and in Appendix A.

[12] The thermal model uses a Galerkin formulation of the finite element method. In the simulations presented here, a modified version of a program developed by *Kohl and Hopkirk* [1995] and *Kohl* [1999] is used to solve the steady state advection diffusion equation for user-defined material properties (heat production, thermal conductivity, density, and specific heat), boundary conditions, and nodal advection velocities that define rock exhumation pathways. The kinematic model simulates heat transfer for each of three exhumation geometries we refer to as ''vertical'' (Figure 2a), ''lateral'' (Figure 2b), and ''thrust'' (Figure 2c). Topography is assumed to remain constant (see section 3.3) such that the vertical component of the velocity field is equivalent to the exhumation rate. As a consequence, the vertical exhumation case considered below is equivalent to purely erosional exhumation of rocks. The other scenarios we consider explore the sensitivity of cooling ages to exhumation during active faulting and lateral rock motion that may characterize deformation in convergent orogenic settings.

[13] The model free parameters are the exhumation geometry and rate (v_z), which we vary from 0.1 to 3.0 mm/yr. All other parameters (surface and basal boundary conditions, radiogenic heat production, thermal conductivity, specific heat, and density) are fixed (Tables 1 and 2). We chose to examine only one fault geometry for the thrust model simulations, similar to the geometry that has been inferred for the MCT system in Nepal [e.g., *Lavé and Avouac*, 2000]. The ramp-flat geometry consists of a deep flat segment and a 28° dipping ramp segment. This geometry allows straight-

Figure 2. Kinematic model and sample location distribution for cooling age predictions. (a) Cartoon block diagram of model domain for ''vertical,'' (b) ''lateral,'' and (c) ''thrust'' exhumation models. Black arrows indicate characteristic rock particle trajectories, white arrows indicate relative vertical component of exhumation for rock particles along a transect in *Y* axis parallel direction, and dashed line indicates schematic position of closure temperature isotherm of interest. (d) Map view example of age-elevation profile ''C.'' Contours depict temperature at the surface in the model domain and are a proxy for elevation because the surface boundary condition is set to reflect an atmospheric lapse rate that is elevation-dependent. C_{yz} is made up of samples collected in the YZ plane, and C_{xz} contains samples collected in the XZ plane. (e) Map view of portion of model domain for which sample ages were predicted. Thick black lines indicate age-elevation profiles at locations A, B, C, D, and E, and stars indicate ''near-vertical'' profile locations I, II, III, IV, and V. River bottom samples include the locations denoted with circles, as well as samples from the other profiles that are located at the river bottom level. Fault location for thrust model in Figure 2c is included for reference. Box outlines region in Figure 2d.

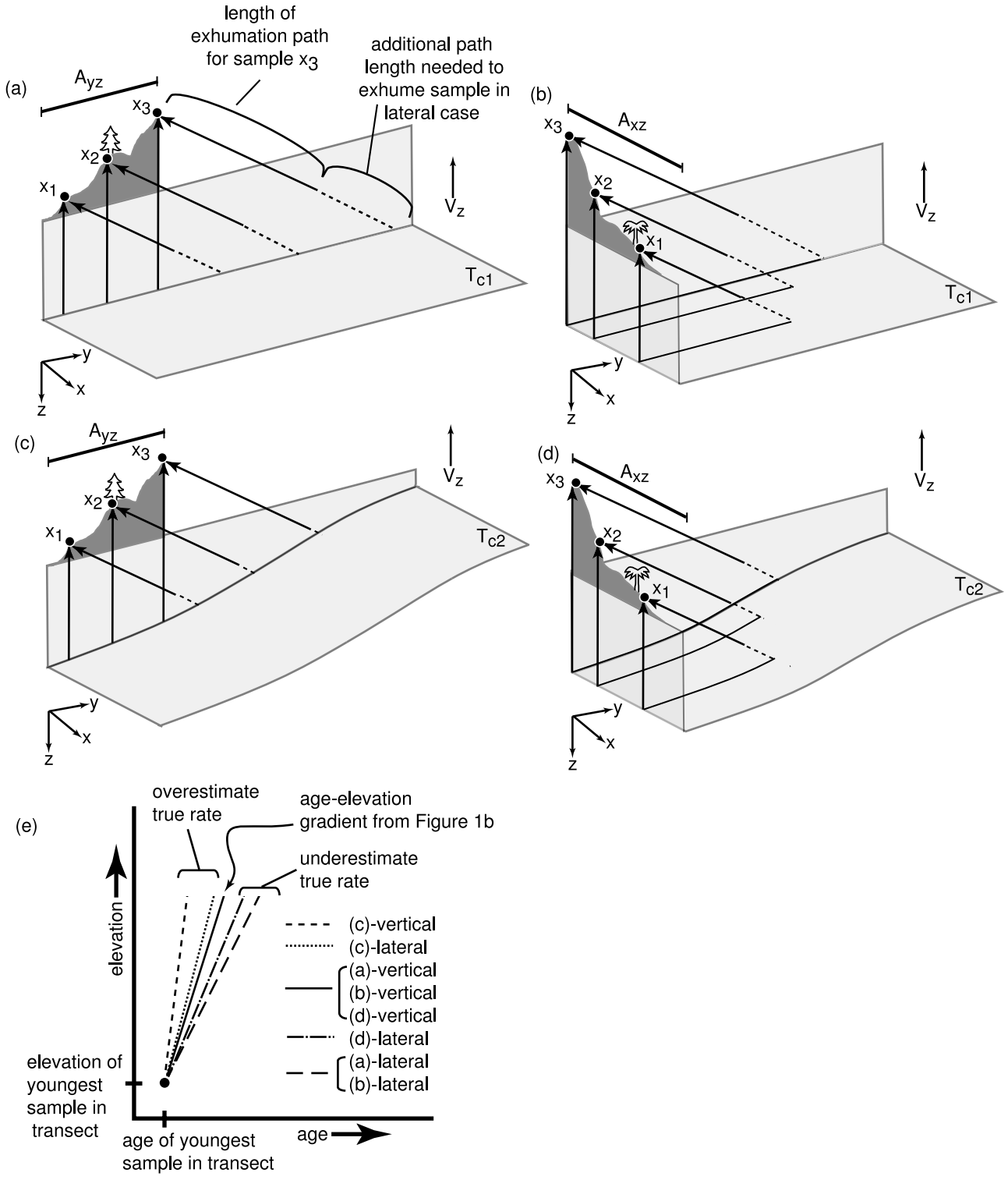
(a)
length of exhumation path for sample x3
additional path length needed to exhume sample in lateral case
Ayz
x3
x2
x1
Vz
Tc1
y
x
z
(b)
Axz
x3
x2
x1
Vz
Tc1
y
x
z
(c)
Ayz
x3
x2
x1
Vz
Tc2
y
x
z
(d)
Axz
x3
x2
x1
Vz
Tc2
y
x
z
(e)
overestimate true rate
age-elevation gradient from Figure 1b
underestimate true rate
elevation
(c)-vertical
(c)-lateral
(a)-vertical
(b)-vertical
(d)-vertical
(d)-lateral
(a)-lateral
(b)-lateral
elevation of youngest sample in transect
age of youngest sample in transect
age

Figure 3

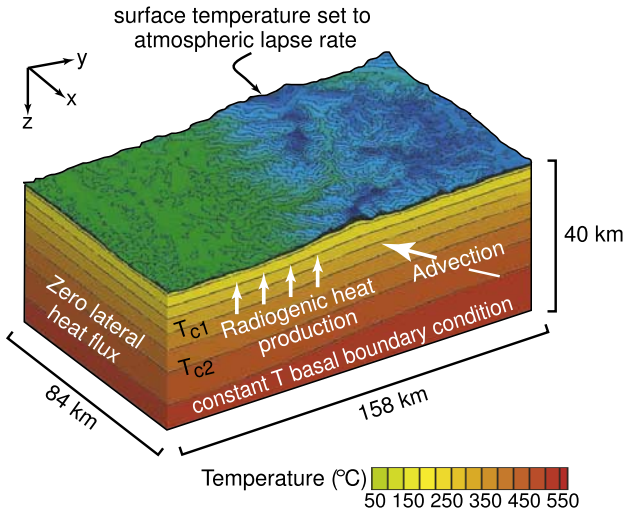

Figure 4. Thermal model domain and boundary conditions. Figure modified after *Whipp et al.* [2007]. Large white arrow indicates example rock path for the lateral kinematic scenario depicted in Figure 2b. Sample passes through closure isotherm for T_{c2} and later passes through closure isotherm for T_{c1}.

forward comparison of results for the thrust and lateral models in order to isolate the effects of rock pathways with significant lateral component from the influence of the thrust fault on the thermal field.

[14] Thermal histories of rocks exhumed to different sample locations (Figures 2d and 2e) were recorded for calculation of cooling-rate-dependent thermochronometer ages. Ages were predicted for the apatite (U-Th)/He (AHe), apatite fission track (AFT), and zircon fission track (ZFT) systems using the TERRA software of *Ehlers et al.* [2005] which calculates closure temperature as a function of cooling rate. Muscovite $^{40}Ar/^{39}Ar$ (MAr) thermochronometer ages were predicted assuming a nominal closure temperature of 350°C, and the general trend in MAr results discussed here is relatively insensitive to this assumption. A series of simulations were conducted (see section 4) with different exhumation rates and trajectories to generate predicted cooling ages at the model surface. The ages are used to examine age-elevation gradients and compare apparent rates with actual rates prescribed by the model.

3.3. Caveats

[15] In order to isolate the effect of exhumation trajectory on cooling ages, we assume that the model topography is static. More complicated treatments of topography (i.e., evolving landscapes) are possible [e.g., *van der Beek and Braun*, 1999], but the influence of exhumation trajectories on cooling ages would be subject to many of the same processes we investigate here for a steady state landscape. This approach is a first step toward identifying how exhumation trajectories might influence age-elevation relationships in eroding regions.

[16] We note that the model results are nonunique and that different combinations of parameters can result in very similar distributions of predicted ages [e.g., *Whipp et al.*, 2007]. Examples of how trade-offs among some of the different parameters investigated here influence predicted age-elevation gradients are discussed in section 5.

4. Results

[17] In this section we present predicted thermochronometer age-elevation profiles for variations in model input parameters and sample profile orientation. We first present results from a simple simulation that documents the effect of vertical exhumation pathway on age-elevation profiles with different orientations across topography. Next, we explore the conditions under which lateral exhumation pathways and thrust faulting cause measurable deviations from the baseline simulations. Results of selected model simulations are summarized in Table 2. A detailed statistical analysis of the difference between age-elevation gradients and true exhumation rates as a function of sample uncertainty follows in section 5.

4.1. Effect of Vertical Exhumation Pathway on Predicted Ages (Baseline Model)

[18] In the absence of active range-bounding structures, rocks are exhumed via erosion and follow vertical exhumation pathways (Figure 2a). Most thermochronometry studies assume this type of geometry. As a consequence, we use a vertical exhumation trajectory as our baseline simulation to explore how variations in the exhumation rate and sample profile orientation with respect to topography influence the apparent exhumation rate, E, derived from the slope of the best fit line through an age-elevation plot (Figures 2d–2e).

Figure 3. Influence of sample profile orientation with respect to closure isotherm geometry and exhumation pathway on age-elevation gradients. (a) Vertical and lateral exhumation paths for samples in age-elevation profile A_{yz}, collected in the YZ plane (in the direction of lateral transport). Closure isotherm (T_{C1}) is horizontal. (b) Age-elevation profile A_{xz}, collected in the orthogonal (XZ) plane. Closure isotherm as in Figure 3a. (c) Age-elevation profile A_{yz}, collected in the YZ plane, in the direction of long-wavelength topography. Elevation (z) of the closure isotherm (T_{C2}) does not vary in the X direction but shallows in the positive Y direction. (d) Age-elevation profile A_{xz}, collected in the orthogonal (XZ) plane. Closure isotherm as in Figure 3c. (e) Age-elevation gradients for the vertical and lateral exhumation scenarios depicted in Figures 3a–3d, each with the same true exhumation rate v_z. Age-elevation lines are normalized by the age and elevation of the youngest sample in each profile to facilitate comparison of slopes.

Table 1. Numerical Model Parameters

Property/Parameter	Model Input Value
Material Properties	
Heat production	0.5 μW/m^3
Thermal conductivity	2.5 W/mK
Specific heat	800 J/kg K
Density	2750 kg/m^3
Numerical Parameters	
Vertical exhumation rate[a]	0.1–3.0 mm/yr
Lateral exhumation angle	28°
Fault segment dip	0°, 28°
Lateral advection rate	0.19–5.6 mm/yr
Fault convergence rate[b]	2 × (0.19–5.6 mm/yr)
Model time step	0.1–0.5 Ma
Horizontal node spacing	700 m
Average vertical node spacing	~1500 m
Surface temperature	14°C–7°C/km × elevation
Basal temperature	600°C
Thermal model domain	84 × 140 × 50 km

[a]Rate at surface at locations for which sample ages are predicted.
[b]Rate of underthrusting equals one half of the total lateral convergence velocity $v_{converge}$, which is set to yield vertical exhumation rates in the hanging wall of the thrust for comparison to the vertical and lateral models.

4.1.1. Vertical Exhumation Model and Thermal Field

[19] In the vertical model simulations, the thermal field beneath the Himalaya is controlled primarily by the rate of exhumation (v_z) and the overlying topography. In these simulations thermal gradients were highly variable beneath ridges and valleys at low exhumation rates and less variable for simulations at high exhumation rates. At an exhumation rate of 0.1 mm/yr average thermal gradients were as low as ~17°C/km. At a higher exhumation rate of 3 mm/yr, thermal gradients were up to 50°C/km. This variation in thermal gradients causes variation in the effective closure temperature depth for different thermochronometers. Vertical exhumation simulations for exhumation rates ≤1.0 mm/yr predict closure depths of ~15–20 km for MAr samples, ~9–14 km for ZFT samples, ~6–12 km for AFT samples, and ~2–6 km for AHe samples. Closure depths are significantly shallower for vertical models with model exhumation rates that exceed this range; the MAr closure depths range from ~7 to 12 km and AHe closure depths range from <1 to 4 km when the model exhumation rate is high (v_z = 3.0 mm/yr).

4.1.2. Age-Elevation Transect Orientation

[20] The final output from the model consists of an array of predicted cooling ages for different thermochronometers sampled along a variety of age-elevation transects (Figure 2e). The age-elevation gradients are sensitive to the topographic slope over which each profile is sampled as well as the surrounding 3-D topography [e.g., *Braun*, 2002a], and the sampling schemes investigated (Figures 2d and 2e) were selected to represent a range of slopes (Table 3) and localities. We start with two end-member scenarios, hereafter referred to as the "near-vertical" and "river bottom" profiles (Figure 2e). The near-vertical profiles comprise sample locations from steep slopes that average 700 m of relief for every 1000 m of horizontal distance (35° slope angle). The river bottom profile represents an elevation

Table 2. Selected Model Simulations

	Vertical Velocity, mm/yr			River Bottom E% Error				Near-Vertical E% Error[a]			
Model	v_x	v_y	v_z	MAr	ZFT	AFT	AHe	MAr	ZFT	AFT	AHe
m101	0.00	0.00	1.00	75	102	125	225	2	2	3	9
m102	0.00	0.00	3.00	120	157	227	492	3	5	7	25
m103	0.00	0.00	0.50	57	72	96	167	2	1	2	6
m104	0.00	0.00	0.10	-	56	74	128	-	6	2	1
	Lateral Velocity, mm/yr			River Bottom E% Error				Near-Vertical E% Error[a]			
Model	v_x	v_y	v_z	MAr	ZFT	AFT	AHe	MAr	ZFT	AFT	AHe
m107	0.00	1.63	1.00	-	29	57	162	-	0	4	4
m108	0.00	4.90	3.00	-	113	178	406	-	4	6	10
m109	0.00	0.81	0.50	-	31	54	165	-	8	4	5
m110	0.00	0.16	0.10	-	25	42	128	-	5	3	4
	Thrust Velocity, mm/yr			River Bottom E% Error				Near-Vertical E% Error[a]			
Model	v_x	$v_{converge}$	$v_{z,max}$	MAr	ZFT	AFT	AHe	MAr	ZFT	AFT	AHe
m111	0.00	1.63	1.00	-	30	57	162	-	1	1	6
m112	0.00	4.90	3.00	-	83	141	327	-	18	4	10
m113	0.00	0.81	0.50	-	26	45	133	-	4	10	6
m114	0.00	0.16	0.10	-	30	41	121	-	7	8	5

[a]E% error computed as $(E - v_z)/v_z \times 100$; results presented in near-vertical section are an average of the near-vertical profiles. Note that $v_{converge} = 2v_y$ for the hanging wall rocks that we track. Also note that error percent does not necessarily vary systematically by exhumation rate and closure temperature because of the local effects of 3-D topography.

Table 3. Average Topographic Slope and Relief of Sample Transects at Locations A, B, C, and D

Location	Orientation	Slope	Degrees	Relief, m
A_{xz}	in XZ plane	0.52	27	2123
A_{yz}	in YZ plane	0.17	10	2953
B_{xz}	in XZ plane	0.56	29	1728
B_{yz}	in YZ plane	0.24	13	3766
C_{xz}	in XZ plane	0.47	25	2313
C_{yz}	in YZ plane	0.25	14	3609
D_{xz}	in XZ plane	0.46	25	3341
D_{yz}	in YZ plane	0.33	18	3987

increase of only 50 m per 1000 m distance, and although such a profile is not appropriate for age-elevation studies we include it for comparative purposes. Because it is difficult to sample near-vertical profiles in the field, we also investigated "intermediate slope" profiles. These profiles, sampled at four locations across the topography denoted A, B, C, and D (Figure 2e), span a much smaller horizontal distance than the river bottom profiles, but are less steep than the near-vertical profiles.

[21] In our model, the long-wavelength (greater than ~100 km) topography varies significantly in the YZ plane as mean elevations increase from the foreland to the range crest. In contrast, long-wavelength topography varies little in the orthogonal direction, parallel to the range crest (XZ plane). Since the influence of long-wavelength topography differs in orthogonal directions, at each of the locations A, B, C and D, we sampled one profile collected in the YZ plane and one profile collected in the XZ plane. Profiles oriented in the direction of the long-wavelength topographic signal (YZ plane) were collected on slopes representing an elevation gain of 170–330 m per 1 km of horizontal distance (10–18° slopes), while profiles oriented in the orthogonal (XZ) plane were sampled on slopes representing an elevation gain of 460–520 m per 1 km of horizontal distance (25–27° slopes; Table 3). As shown in Figures 3a–3d and Figure 2d, we refer to sample profiles in the XZ plane with the subscript *xz*, and sample profiles in the YZ plane with the subscript *yz*.

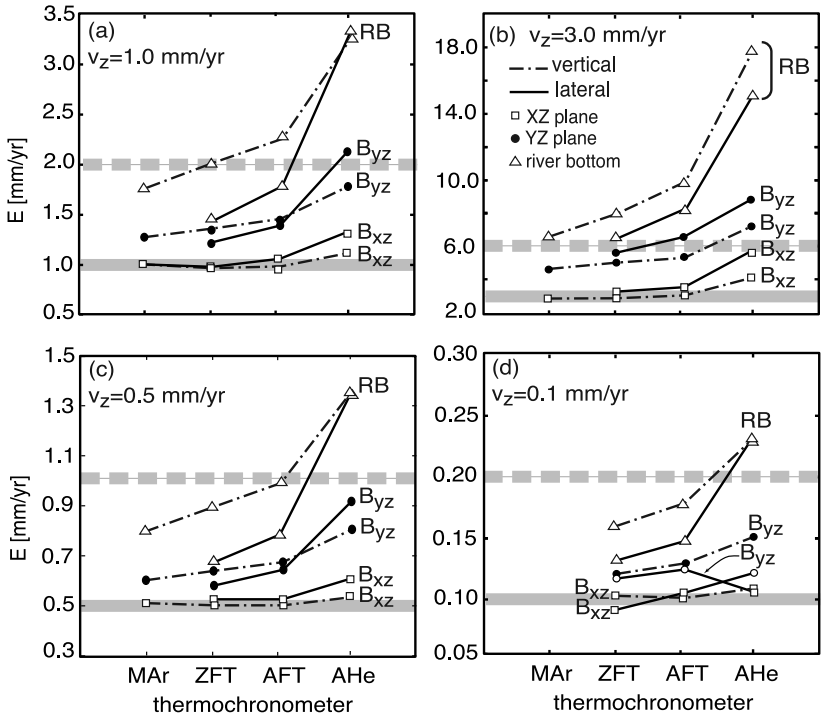

Figure 5. Age-elevation gradient (E) for river bottom samples and samples in the orthogonal age-elevation profiles at location B. MAr, muscovite $^{40}Ar/^{39}Ar$; ZFT, zircon fission track; AFT, apatite fission track; and AHe, apatite (U-Th)/He thermochronometer results. River bottom samples are labeled RB (triangles), and samples in age-elevation profile B are labeled B_{xz} (squares, profile collected in the XZ plane) and B_{yz} (solid circles, profile collected the in YZ plane, in the direction of the long-wavelength topographic variation). Dash-dotted lines indicate results for vertical exhumation models and solid lines indicate results for lateral exhumation models. (a) Model exhumation rate v_z = 1.0 mm/yr, (b) v_z = 3.0 mm/yr, (c) v_z = 0.5 mm/yr, and (d) v_z = 0.1 mm/yr. Thick grey line indicates v_z. Thick dashed grey line indicates $2*v_z$ for reference.

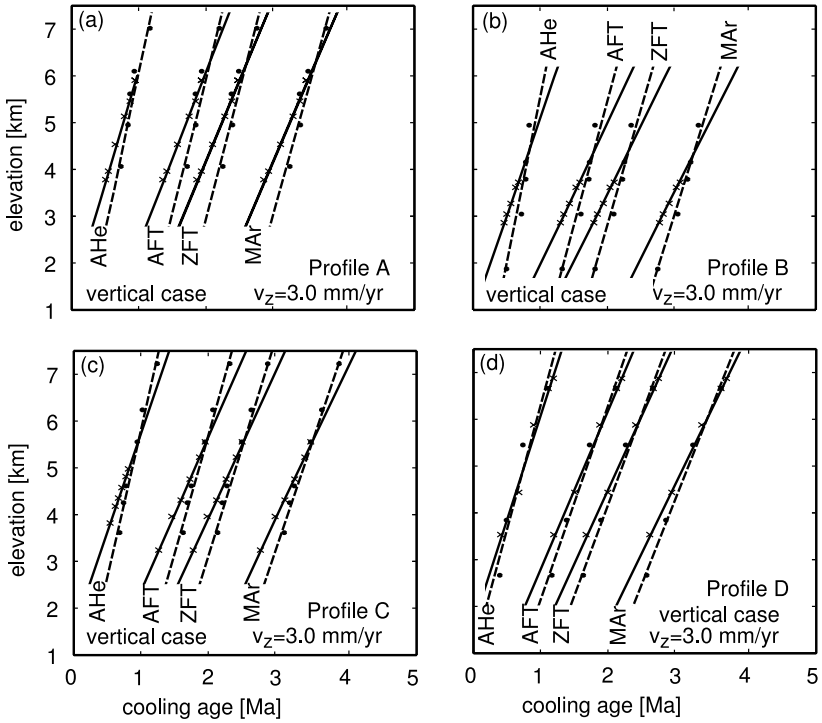

Figure 6. Comparison of age-elevation plots for orthogonal profiles in different locations (vertical exhumation pathways, model exhumation rate v_z = 3.0 mm/yr). Profiles collected in the XZ plane denoted with crosses and black best fit lines. Age-elevation gradients for orthogonal profiles (in YZ plane), collected in the direction of long-wavelength topography, are denoted with solid circles and best fit is denoted with dashed lines. Profile locations (a) A, (b) B, (c) C, and (d) D. Locations are shown in Figure 2e. Thermochronometer notation is as in Figure 5.

4.1.3. Influence of Closure Temperature on Apparent Exhumation Rates

[22] The influence of exhumation rate and sample profile orientation on apparent exhumation rates (E) interpreted from age-elevation gradients is greatest for low-temperature thermochronometers. A comparison of apparent exhumation rates for the four vertical exhumation simulations shown in Figure 5 (dash-dotted lines) reveals that the AHe thermochronometer generally provides larger overestimates of the model exhumation rate than the higher-temperature thermochronometers. For each of the simulations shown in Figure 5, AHe age-elevation gradients for the different sample profile types (river bottom profiles and location B profiles oriented in the XZ and YZ planes) also yield a greater range of apparent rates than the other thermochronometers we examined. Both the worst rate overestimates and largest spread of apparent rates occur for the AHe thermochronometer in the most rapid exhumation model (Figure 5b), with the apparent exhumation rate from the river bottom AHe profile being almost nine times greater than the model exhumation rate. The error is largest for the AHe and AFT systems because topographic perturbations to the thermal field are greatest at shallow crustal depths where these thermochronometers are most sensitive. The error increases with increased exhumation rates above ~0.5 mm/yr (e.g., compare Figures 5a and 5c) for all thermochronometers because higher exhumation rates cause shallower closure temperature depths where topographic disturbances to the thermal field are more significant.

4.1.4. Influence of Profile Steepness on Apparent Exhumation Rates

[23] The topographic slope over which samples are collected has a strong influence on exhumation rate estimates from age-elevation gradients. Steep profiles generally return the most accurate rate estimates for the vertical exhumation simulations. Representative results for the six near-vertical profiles we examined are listed in Table 2 and can be summarized as follows: at a moderate model exhumation rate (v_z = 1.0 mm/yr), the average difference between the model and apparent rates is small – less than 3% for the MAr, ZFT, and AFT thermochronometers, and <10% for the AHe thermochronometer. At higher rates (v_z = 3.0 mm/yr), the average difference between the model and apparent rates increases significantly to ~3%, 5%, 7%, and 25% for the MAr, ZFT, AFT, and AHe thermochronometers, respectively. For the slowest vertical exhumation cases (v_z = 0.1 mm/yr), the average difference between the model and apparent rates remains small (less than ~6% for all thermochronometers). These results highlight the fact that when age-elevation profiles are sufficiently steep, the model and apparent rates agree relatively well. This finding is consistent with those of *Stüwe et al.* [1994] for regions of

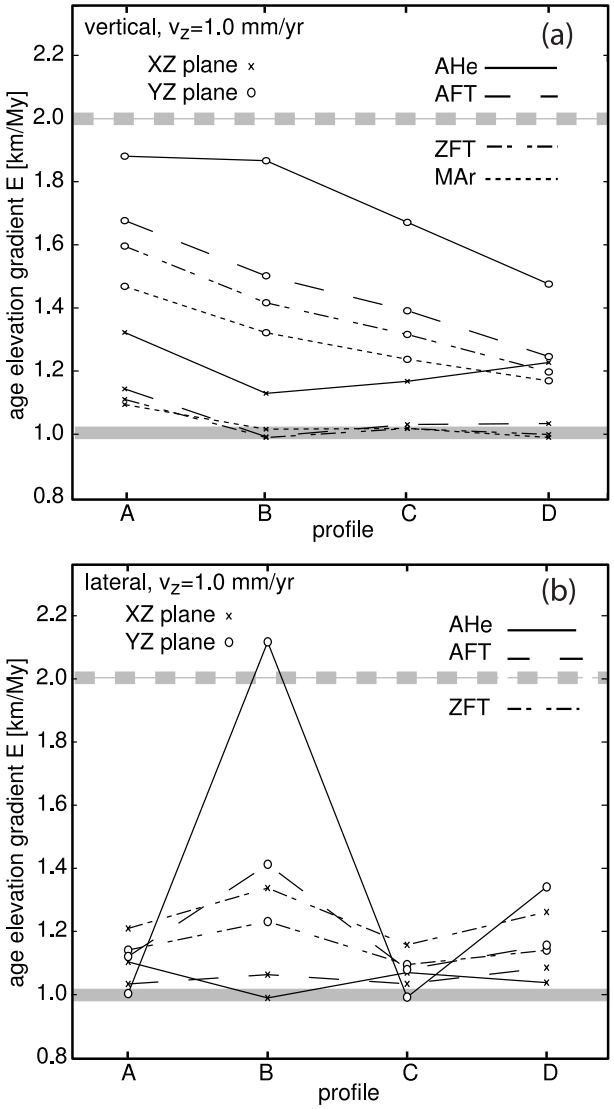

Figure 7. Variation in age-elevation gradients for orthogonal profiles by location (A, B, C, and D shown in Figure 2e). Results for profiles collected in the XZ plane denoted with x's, and results for profiles collected in the YZ plane denoted with circles. Line type (see legend) indicates thermochronometer type. (a) Vertical exhumation model with exhumation rate v_z = 1.0 mm/yr, and (b) lateral exhumation model with v_z = 1.0 mm/yr. Thick grey line indicates v_z, and dashed thick grey line indicates $2*v_z$.

high relief and short-wavelength topography. In contrast, the difference between apparent and real exhumation rates dramatically increases when samples are collected over a large lateral distance like the river bottom sample profiles (Figure 5 and Table 2). River bottom apparent exhumation rates are up to 6 times greater than the model rate when exhumation is rapid (Figure 5b), and apparent rates for the thermochronometers we examined are still only within 128% of the model rate when exhumation is gradual (v_z = 0.1 mm/yr) (Table 2). Although the difference between the model and apparent exhumation rates decreases for slower exhumation rates and for higher-temperature thermochronometers, river bottom profiles in the vertical exhumation simulations do not produce age-elevation gradients that come within 50% of the actual exhumation rate in the model.

4.1.5. Influence of Profile Orientation on Apparent Exhumation Rates

[24] Predicted age-elevation gradients for the vertical exhumation simulations discussed in this section vary by profile orientation with respect to the long-wavelength topography and by location on the landscape (Figures 5, 6, and 7). In all of the vertical exhumation simulations (model exhumation rates from v_z = 0.1–3.0 mm/yr), sample profiles oriented parallel to the long-wavelength topography (YZ plane) provided worse estimates than profiles oriented in the orthogonal direction (XZ plane). This relationship between age-elevation gradients from orthogonal sample profiles, shown in Figure 6 for a case of rapid exhumation at 3.0 mm/yr, holds for all thermochronometers and all locations we examined on the landscape. For the MAr, ZFT, and AFT systems, apparent exhumation rates for most profile locations (B, C, and D) are within 2% of the model rate for age-elevation transects collected orthogonal to the long-wavelength topography (in the XZ plane) over a wide range of exhumation rates (v_z = 0.1–3.0 mm/yr). In contrast, the difference between model and apparent exhumation rates for these thermochronometers and locations increases to 15–45% for transects oriented parallel to the long-wavelength topography. For the same range of model rates, profiles collected at location A provide much less accurate rate estimates than profiles collected at B, C, and D: apparent exhumation rates for profile A samples collected perpendicular to the long-wavelength topography (in the XZ plane) are within 8–12% of the model exhumation rate, and samples collected in the orthogonal profiles (in the YZ plane) overestimate the model exhumation rate by 42–60% (Figure 7a).

[25] To first order, we might expect that the difference between apparent exhumation rates for orthogonal profiles can be explained simply by the difference in topographic slope over which they were collected; profiles oriented parallel to the long-wavelength topography (in the YZ plane) were collected along shallower slopes than profiles in the orthogonal (XZ) plane (Table 3). However, a detailed examination of the variation of age-elevation gradients from orthogonal profiles in different locations suggests that although local topographic slope can explain most of the variation, it is not the only influence (Figure 8). For the vertical exhumation simulation results shown in Figure 8 (model exhumation rate of v_z = 1.0 mm/yr), the difference between the model and apparent exhumation rates generally decreases as the topographic slope of the age-elevation transect increases. However, the relationship is not always monotonic. While the age-elevation gradient given by the AHe thermochronometer actually provides a worse rate estimate when collected over a topographic slope of 27° than it does over a slope of 25°, the apparent exhumation rate for this thermochronometer varies little between a topographic slope of 10°

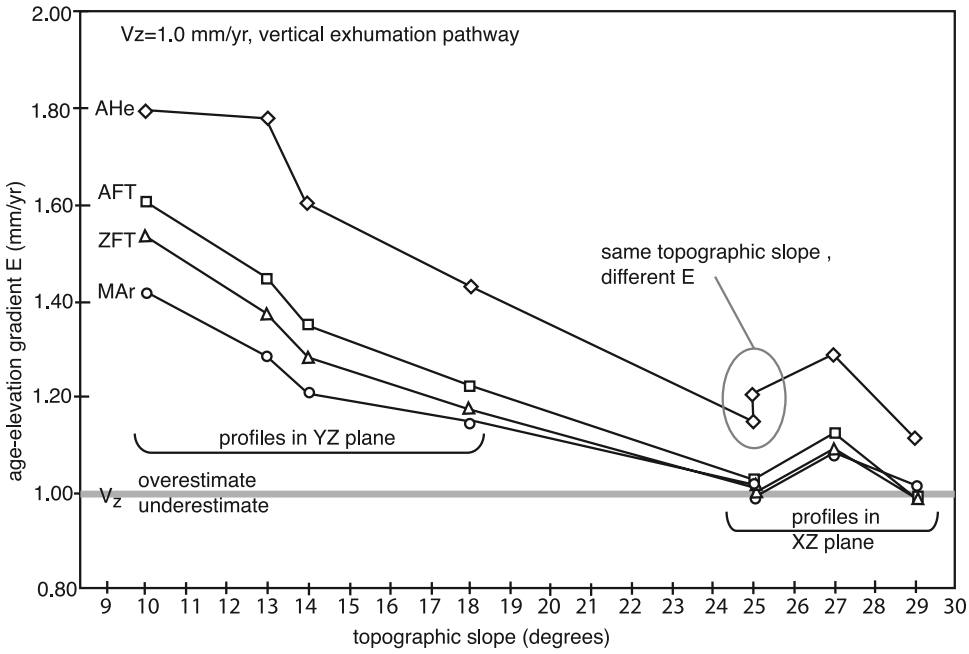

Figure 8. Age-elevation gradient (E) as a function of average local topographic slope over which the profile was sampled. Results shown for vertical exhumation simulation with a model exhumation rate v_z = 1.0 mm/yr. AHe (diamonds), AFT (squares), ZFT (triangles), and MAr (circles) age-elevation gradients shown orthogonal transect orientations in samples locations A, B, C, and D (Figure 2e). Grey line indicates model exhumation rate v_z; results that plot above this line overestimate the exhumation rate, and results that plot below this line underestimate it. Note the two circled diamonds that indicate two profiles collected over the same topographic slope with different age-elevation gradients.

and 13°. Although sample profiles oriented orthogonal to the long-wavelength topography (in the XZ plane) at both locations C and D have a topographic slope of 25° (Table 3), they yield different age-elevation gradients (Figure 8). These observations suggest that even when samples are exhumed along vertical pathways, 3-D topographic variations around each profile also influence the age-elevation gradient for a given thermochronometer.

[26] The magnitude of the difference between the model and apparent exhumation rates for a given thermochronometer, profile location, and profile orientation with respect to the long-wavelength topography increases for faster model exhumation rates, and decreases for slower rates. For a profile collected over a topographic slope of 10° in the direction of the long-wavelength topographic signal (YZ plane), the age-elevation gradient overestimates the model exhumation rate by up to ~5 mm/yr when exhumation is rapid and by less than 1 mm/yr when exhumation is more gradual. Regardless of the model exhumation rate, the magnitude of the rate estimate error decreases for the higher-temperature thermochronometers. In terms of percent error, the difference between model and apparent exhumation rates also decreases with increasing closure temperature.

4.2. Effect of Lateral Exhumation on Predicted Ages

[27] Age-elevation gradients are subject to the same effects of topography and erosion when rocks are exhumed laterally as they are when vertical exhumation occurs strictly via erosion. Additional effects of horizontal rock transport during exhumation are discussed in the following paragraphs, where we simulate results for a simplified oblique exhumation geometry that does not include faults.

4.2.1. Lateral Exhumation Model and Thermal Field

[28] In the lateral exhumation simulations, rocks remain stationary with respect to the *X* axis, but change position with respect to the Y and Z axes as they are exhumed to the surface at an angle of 28° from the horizontal. The near-surface thermal field and closure depths for the lateral models deviate somewhat from those of the vertical models. For example, the closure depth for river bottom samples changes by an average of 0.25 km (~23%) when exhumation is rapid (v_z = 3.0 mm/yr). AHe closure depths change by ~10% for model exhumation rates of 0.1 mm/yr, and the difference decreases for higher-temperature thermochronometers.

4.2.2. Age-Elevation Gradients in the Lateral Exhumation Simulations

[29] Lateral transport can partly counteract the tendency of age-elevation gradients to overestimate exhumation rates due to topographic effects for some profile orientations (e.g., Figure 3c). As a consequence, lateral rock motion results in a lower misfit between the model and apparent exhumation rates than we observe when exhumation is vertical for some of the sample profiles we examined. For example, at moderate exhumation rates (v_z = 1.0 mm/yr),

near-vertical sample profiles provide better exhumation rate estimates when exhumation is lateral than when exhumation is vertical, overestimating the model rate by averages of 0–4% and 2–9% for these cases, respectively. River bottom age-elevation gradients also provide better rate estimates in the lateral exhumation simulations than in the vertical exhumation simulations for all but the AHe thermochronometer (Figure 5 and Table 2).

[30] The difference between the model and apparent rates as a function of lateral transport is sensitive to the exhumation rate. For the near-vertical sample profiles, the difference between the model and apparent exhumation rates increases when exhumation is rapid (v_z = 3.0 mm/yr), such that near-vertical profiles provide rate estimates that are within 4–10% of the model rate for all thermochronometers, compared to up to 25% error for the estimate from the vertical exhumation case. At moderate exhumation rates ($v_z \leq$ 1.0 mm/yr), apparent rates for intermediate-slope profiles oriented parallel to the long-wavelength topography (in the YZ plane) also more closely approximate the model rate when rocks are exhumed laterally with the exception of the AHe thermochronometer (Figures 5a and 5c). For rapid exhumation rates (v_z = 3.0 mm/yr) however, age-elevation gradients for the same profiles provide worse rate estimates in the lateral exhumation simulations than in the corresponding vertical cases (Figure 5b).

[31] The difference in age-elevation gradients as a function of lateral transport is sensitive to the profile orientation with respect to the transport direction, reflecting the competing effects of lateral transport and topography. While lateral transport improved apparent rate estimates for profiles oriented parallel to the long-wavelength topography (in the YZ plane) for some cases, on average, apparent rates for profiles oriented orthogonal to the long-wavelength topography (in the XZ plane) were similar for the vertical and lateral exhumation scenarios. Although they differ by 25% for the AHe thermochronometer and by 5% for the other systems we examined, rate estimates for these profiles do not improve when rocks are exhumed laterally (Figure 5).

4.3. Effect of Thrust Faulting on Predicted Ages

[32] It is well known that crustal-scale thrust faults significantly influence the subsurface thermal field [e.g., *Bird et al.*, 1975]. In order to gain additional insight into the potential magnitude of this effect on our predicted age-elevation gradients, we incorporated a structural discontinuity into the model simulations discussed in this section.

4.3.1. Thrust Model and Thermal Field

[33] For the thrust model simulations we chose a fault geometry similar to the MCT system in central Nepal, thought to be a major structural and metamorphic discontinuity in the study region. In the thrust model simulations, geographic coordinates are set so that rocks in the footwall travel in the positive Y direction and rocks in the hanging wall travel in the negative Y direction while remaining fixed with respect to the *X* axis (Figure 2c). Footwall rocks are not exhumed as they are transported toward the fault, and the model exhumation rate (v_z) in the footwall is 0.0 mm/yr. The rate of underthrusting is set to equal one half of the total lateral convergence velocity, and the model exhumation rate in the hanging wall varies with distance as the dip of the fault changes, as described in Appendix A (equation (A3)). Rocks are exhumed at the maximum exhumation rate in the immediate hanging wall of the thrust (above the ramp segment with a dip of 28°). As all of the rocks we tracked were sampled from above the ramp, the model exhumation rate at the surface for each point is the same for corresponding lateral and vertical exhumation simulations (Table 2).

[34] The thermal field in the thrust models is influenced by lateral heat flow across the fault as well as lateral heat flow owing to topography. Such thermal effects of thrust faulting have been investigated by a variety of workers [e.g., *Oxburgh and Turcotte*, 1974; *Bird et al.*, 1975; *Toksoz and Bird*, 1977; *Ruppel and Hodges*, 1994]. When crustal-scale thrust faults are active, the juxtaposition of hot hanging wall material and cold footwall material drives heat flow across the boundary, causing closure isotherms to become curved (Figure 2c). When fault slip rates are rapid enough, this effect may perturb the thermal field significantly. As the temperature difference between the hanging wall and footwall increases with increasing slip rate, the contrast drives more heat flow and depresses the geothermal gradient in the hanging wall. Although in natural convergent settings frictional heating due to fault slip, redistribution of radiogenic heat producing material, topographic development, and topographically driven fluid flow may also be important [e.g., *Ehlers*, 2005; *Whipp and Ehlers*, 2007], we include only frictional heating in our steady state simulations (see Appendix A).

[35] We find that the thermal field in the thrust simulations is significantly different from the thermal field in the lateral exhumation simulations when the slip rate across the fault is rapid. Because the exhumation rate in the hanging wall of the thrust is a function of the slip rate in our model (Appendix A), this effect is manifested at rapid model exhumation rates. Although we do not show the thermal models here, we note that closure depths for river bottom samples are roughly twice as deep in the thrust simulations as they are in the lateral exhumation simulations when fault slip is rapid (for model exhumation rates of 3.0 mm/yr in the immediate hanging wall of the thrust) due to significant lateral heat flow across the fault. When slip is moderate and model exhumation rates are less than or equal to ~1.0 mm/yr, the difference in closure depths for the lateral and thrust simulations is reduced to an average of <0.75 km, or 14%.

4.3.2. Age-Elevation Gradients

[36] Age-elevation gradients are similar for lateral and thrust simulations except when significant heat flow across the fault occurs due to rapid slip. This is not surprising given the similarities between the exhumation pathways for the lateral exhumation and thrust simulations. The similarity in apparent rates is evident in a comparison of results for river bottom predicted ages for the two sets of simulations (Table 2). While river bottom age-elevation gradients from thrust and lateral exhumation simulations differ by up to 79% when exhumation is rapid (v_z = 3.0 mm/yr), they are in many cases identical for less rapid exhumation rates

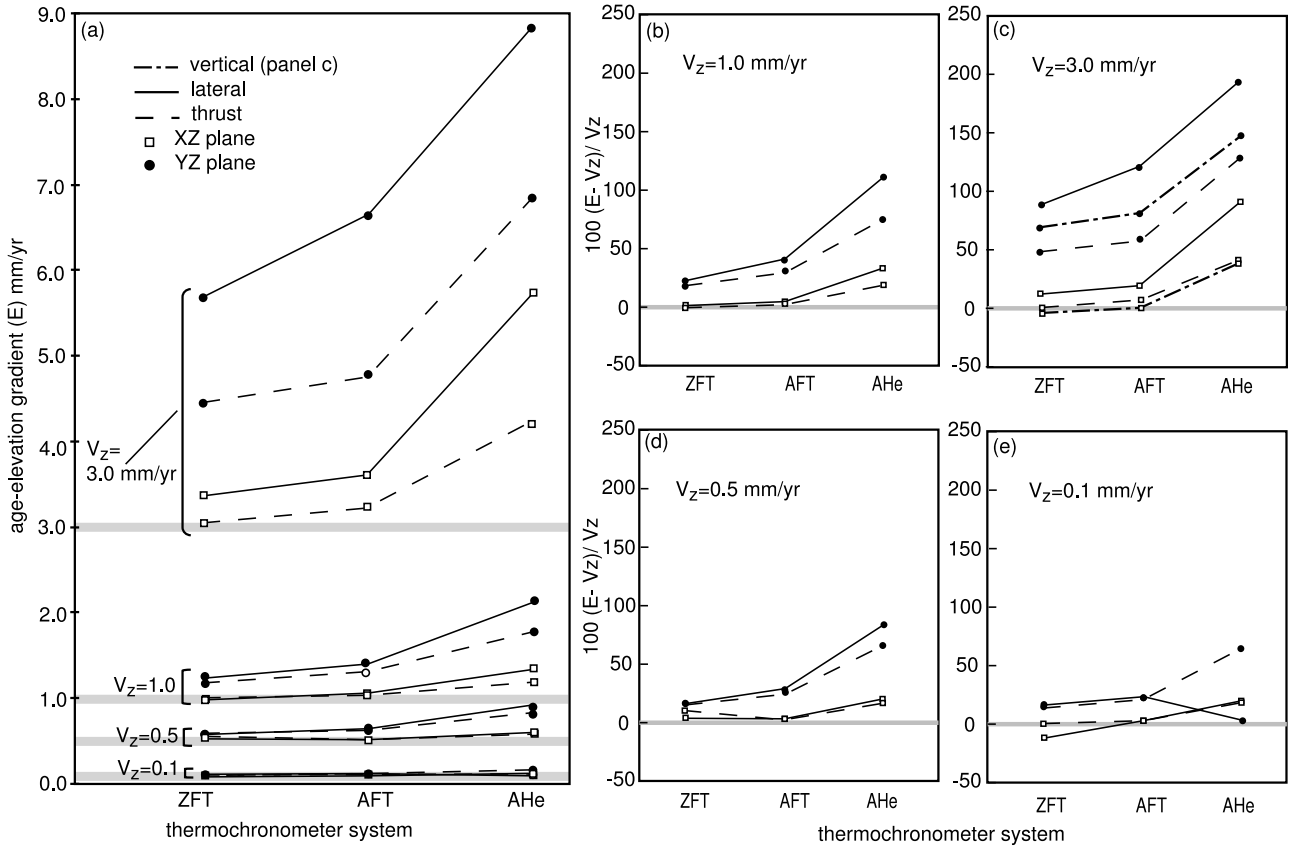

Figure 9. Difference between age-elevation gradients (E) for thrust and lateral exhumation simulations. Profile location B, model exhumation rates (v_z) of 0.1, 0.5, 1.0, and 3.0 mm/yr. (a) Thrust and lateral results for a range of rates on the same scale. Thick grey lines are labeled with model exhumation rate v_z for each set of apparent exhumation rate results. (b–e) Same results, plotted in terms of percent difference from the model exhumation rate. Figure 3c shows vertical models results for an exhumation rate of v_z = 3.0 mm/yr shown for comparison. A subset of these results is also presented in Figure 5.

(Table 2). Although age-elevation gradients for the lateral exhumation and thrust simulations differ somewhat, in all but one case, apparent exhumation rates for the near-vertical profiles are within 10% of the model exhumation rate for both exhumation geometries (Table 2).

[37] For intermediate-slope profiles, the difference between age-elevation gradients for thrust and lateral exhumation simulations is very sensitive to the exhumation rate, and the effect of profile orientation with respect to the transport direction is similar for the two exhumation geometries. The difference in apparent exhumation rates for the two exhumation pathways increases with increasing fault slip and exhumation rate, both in terms of magnitude (Figure 9a) and in terms of the percent error in exhumation rate estimates (Figures 9b–9e). In the most extreme case examined here – a model exhumation rate of 3.0 mm/yr for the AHe thermochronometer–age-elevation gradients for the lateral exhumation and thrust simulations differ by a maximum of ~75% (Figure 9c). At lower slip and exhumation rates for the AFT and ZFT thermochronometers, however, age-elevation gradients for lateral exhumation and thrust simulations can differ by less than a percent (e.g., Figures 9b, 9d, and 9e). When exhumation is sufficiently rapid (>0.5 mm/yr) age-elevation gradients provide better rate estimates for the thrust simulations than for the lateral exhumation simulations (Figures 9a and 9c). However, when exhumation is very slow (0.1 mm/yr) the relationship is more complicated (Figure 9e).

5. Discussion

[38] The magnitude of error in apparent exhumation rates is affected by topography, exhumation rate and pathway, and the steepness, location, and orientation of sample profiles. We find that the sensitivity of apparent age-elevation gradients varies greatly as a function of sample uncertainty when natural samples are considered. Traditionally, the percent error in apparent exhumation rates from

model predictions has been compared with the percent uncertainty in thermochronometer ages or in the best fit slope through an array of age-elevation data to evaluate the likelihood that simplifying assumptions will compromise geologic rate interpretations. However, the analysis in section 5.2 indicates that a more sophisticated approach to determining the significance of the exhumation rate errors predicted by the model is warranted.

5.1. Influence of Exhumation Pathway on Age-Elevation Relationships

5.1.1. Near-Vertical Age-Elevation Profiles

[39] Age-elevation gradients from vertical profiles (i.e., cliff faces) should provide an accurate proxy for exhumation rate as long as the depth of the closure isotherm beneath the vertical profile does not change while samples are passing through it. This condition is met in steady state models. As anticipated, near-vertical age-elevation profiles provide good exhumation rate estimates, with the best estimates being for higher-temperature thermochronometers (Table 2). For near-vertical profiles, samples with exhumation pathways that have a significant component of lateral transport actually provide better rate estimates using the age-elevation method than samples with vertical exhumation pathways for exhumation rates faster than ~1.0 mm/yr (Table 2). While the influence of topographic relief has the effect of causing age-elevation gradients to overestimate exhumation rates [*Stüwe et al.*, 1994; *Mancktelow and Grasemann*, 1997], the influence of lateral exhumation paths has the opposite effect in some cases when sample profiles are not oriented orthogonal to the direction of the lateral component of transport (e.g., Figure 3). For the slowest exhumation rates we examined (0.1 mm/yr), the age-elevation gradients for near-vertical sample profiles are very similar regardless of exhumation pathway, all within 8% of the actual rate (Table 2). This suggests that near-vertical transects are relatively insensitive to the influences of topographic relief and lateral rock transport at these slow rates. In contrast, lateral, vertical, and thrust exhumation pathways result in significantly different age-elevation gradients for near-vertical sample profiles at higher exhumation rates (Table 2). The observation that these apparent rates always overestimate the exhumation rate indicates that topographic effects still tend to outpace the effects of lateral exhumation pathways when exhumation is rapid.

5.1.2. River Bottom Age-Elevation Profiles

[40] Age-elevation gradients from river bottom samples provide the worst exhumation rate estimates observed (Table 2). Although this type of sampling scheme is not appropriate for age-elevation studies, the model predictions for these samples are useful for examining relative differences in age-elevation gradients as a function of exhumation pathway. AHe river bottom profiles result in age-elevation gradients that are essentially the same for vertical and lateral exhumation pathways, except in higher exhumation rate simulations (>0.5 mm/yr). The remaining thermochronometers return rate estimates that are up to three times better for models that incorporate lateral advection over the range of exhumation rates examined here (Table 2). River bottom ZFT, AFT, and AHe age-elevation gradients from thrust and lateral exhumation simulations are remarkably similar at model exhumation rates of less than ~3 mm/yr. The river bottom sample locations are widely spaced over a large area (~60 km; Figure 2e), and the age-elevation gradient they define appears to be relatively insensitive to short-wavelength (valley to adjacent ridge) topographic relief. Instead, the tendency of the river bottom profiles to severely overestimate the exhumation rate may reflect the thermal influence of the long-wavelength elevation increase from the foreland to the core of the range. Because the lateral component of the exhumation pathway for the thrust and lateral exhumation simulations is oriented in the direction of this dominant long-wavelength topographic influence (in the YZ plane), lateral rock transport tends to reduce rate estimate error. A simple explanation for the observation that AHe age-elevation profiles for fast rates are an exception to this pattern (e.g., Figure 5b) is that isotherms corresponding to AHe closure depths beneath a given profile shallow when exhumation is rapid, so the AHe samples are more sensitive to local topography than they are to the foreland-to-range-crest elevation increase and exhumation pathway [*Batt and Brandon*, 2002].

5.1.3. Effect of Profile Orientation With Respect to Long-Wavelength Topography

[41] The intermediate-slope profiles (Table 3) are useful for examining how age-elevation gradients vary as a function of profile orientation with respect to long-wavelength topography and the lateral transport direction. For a given thermochronometer in the vertical exhumation simulations, profiles oriented parallel to the long-wavelength elevation rise from the foreland to the range crest (in the YZ plane) always provide worse rate estimates than orthogonal profiles (Figure 7a). Local topographic slope influences the sensitivity of age-elevation profiles to nonhorizontal closure isotherms, and for the vertical exhumation models, most of the difference between age-elevation gradients for these orthogonal profiles may be attributed to the fact that the profiles in the YZ plane were collected along shallower slopes (Table 3). However, not all of the difference between orthogonal profiles can be attributed to local topographic slope (Figure 8). In our model domain, long-wavelength topographic variation (foreland to range crest) strongly influences the thermal field near closure depths in the YZ plane, while shorter-wavelength topographic variations (valley-ridge elevation differences) influence the thermal field in both the XZ and YZ planes. As a consequence, some of the difference between age-elevation gradients for profiles in the YZ and XZ planes in the vertical exhumation simulations that cannot be explained by a difference in local topographic slope might be explained by the influence of local 3-D topography on closure isotherms.

[42] In comparison to the vertical exhumation simulations, the relationship between profile orientation and age-elevation gradient for the lateral exhumation pathway samples is less straightforward (e.g., Figure 7b), as age-elevation gradients for orthogonal profiles may be expected to differ even in the absence of topographic effects (Figures 2c–2d). For profiles that are oriented perpendicular to the transport direction,

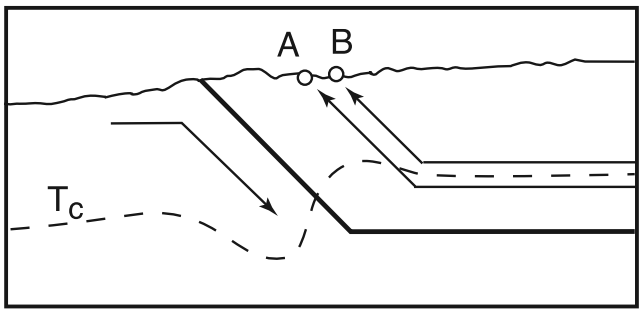

Figure 10. Cartoon of two adjacent samples with very different cooling histories due to the interaction of rock exhumation pathways and the closure isotherm geometry. While sample A crosses the closure isotherm during exhumation, sample B remains above the closure isotherm as it travels to the surface. As a result, sample A is reset for the thermochronometer of interest while sample B is not.

samples with vertical exhumation pathways still provide better rate estimates than samples with lateral exhumation pathways for all but the slowest exhumation rates (e.g., Figure 5). When exhumation is very slow (0.1 mm/yr), higher-temperature thermochronometers can slightly underpredict the real exhumation rate for profiles in this orientation (in the XZ plane) (e.g., ZFT B_{xz} in Figure 5d). The difference between lateral and vertical exhumation pathways is more complicated for the profiles collected parallel to the transport direction (in the YZ plane). In these cases, the exhumation pathway that results in a better rate estimate depends on the profile location (e.g., Figure 7) and the model exhumation rate.

[43] In both the vertical and lateral exhumation simulations, apparent exhumation rates derived from profiles collected on intermediate topographic slopes (Table 3) vary as a function of location across the 3-D landscape (Figure 7b). For the moderate rate lateral exhumation simulation (1.0 mm/yr, Figure 7b), AFT samples collected perpendicular to the long-wavelength topography (in the XZ plane) provide a better proxy for the model exhumation rate than the profiles in the YZ plane at all four locations (A, B, C, and D). However, the difference between age-elevation gradients for orthogonal profiles varies greatly from location to location. The AHe apparent exhumation rate for samples collected in the YZ plane is closer to the model exhumation rate than the apparent exhumation rate for the profile in the XZ plane at locations A and C. However, the opposite is true at locations B and D, and this variability cannot be explained simply as a function of local topographic slope (Table 3). Figure 7b suggests that the variability in age-elevation gradients as a function of position on the landscape is especially large for the AHe thermochronometer, probably because shallow isotherms are most sensitive to short-wavelength local topography. Results for lateral exhumation simulations over a range of model exhumation rates (0.1–3.0 mm/yr) indicate that this variability increases with increasing exhumation rate, and decreases for higher-temperature thermochronometers.

[44] If lithology, outcrop, and access permit, collecting samples along a nearly vertical profile or cliff face is ideal for avoiding complications due to the influence of topography. Although it is well known that collecting steep profiles is advantageous for exhumation-rate studies, *Braun* [2002a, 2002b] alluded to the fact that different types of sample profiles are well suited for relief evolution and exhumation rate investigations. The results of our study suggest that, if lateral transport is known to be significant, profiles oriented orthogonal to the transport direction and long-wavelength topography are likely to be insensitive to this influence even if they are collected across moderate topographic slopes.

[45] The reverse is also true: The model simulations indicate that lateral rock motion can result in a lower misfit between model and apparent exhumation rates when sample profiles span some horizontal distance along the direction of transport. In some cases the tendency of lateral transport to cause rate underestimates balances the tendency of topographic effects to cause rate overestimates, and the apparent exhumation rate closely approximates the true vertical component of exhumation. However, this close agreement is fortuitous in the sense that the apparent rate calculation assumes purely vertical motion and a 1-D static thermal field. Obviously, rock motion is not strictly vertical in the lateral simulations, and the thermal field varies in 3-D. Thus workers interpreting apparent exhumation rates in these settings might get the right answer (for the wrong reason), but not have any information about equally plausible alternative kinematic scenarios without the aid of numerical modeling.

5.1.4. Variation of Age With Structural Elevation Not Related to Exhumation Rate

[46] Not all gradients in age-elevation space represent erosional exhumation. If a pulse of unroofing exhumes a previously stable crustal section spanning the AFT partial annealing zone (PAZ) [e.g., *Brandon et al.*, 1998; *Gleadow and Duddy*, 1981] or the AHe partial retention zone (PRZ) [*Wolf et al.*, 1998], a transect at the surface may include samples from within the PAZ or PRZ with age-elevation relationships that reflect the preunroofing thermal structure rather than the exhumation rate [e.g., *Stockli et al.*, 2000]. Advective heat transport by topography-driven groundwater flow can also modify closure isotherm geometry and age-elevation gradients [e.g., *Whipp and Ehlers*, 2007]. Alternatively, it is possible that complications may arise as a result of the interaction between closure isotherms and nonvertical exhumation pathways. The influence of thrust faults on exhumation paths will vary significantly if the thrust geometry (e.g., fault surface shape or ramp depth) is varied or if multiple faults are active. For hanging wall samples, depending on the fault geometry and exhumation kinematics, two rocks collected beside one another could have experienced very different cooling histories (Figure 10), producing an age-elevation relationship that does not reflect a single exhumation rate. Although we were able to avoid this complication in our modeling study by using a very thick thrust sheet geometry and by only tracking samples in the immediate hanging wall of the fault, in natural

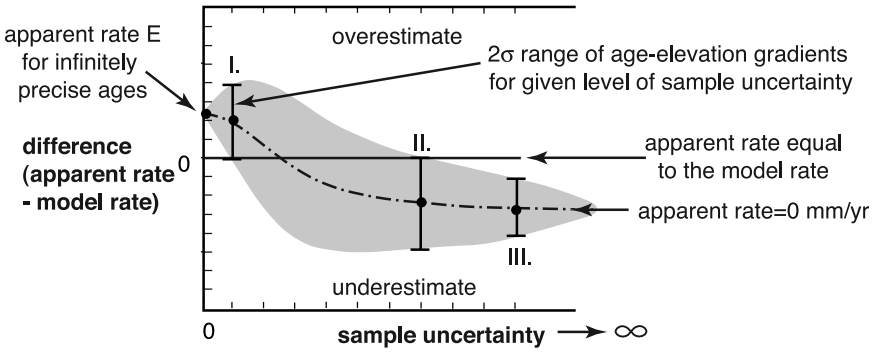

Figure 11. Cartoon of the difference between apparent and model exhumation rates as a function of sample uncertainty. Horizontal line indicates where the apparent exhumation rate equals the model exhumation rate. The black dots labeled I and II indicate mean of distribution of E_n values from Monte Carlo simulations, and error bars indicate 2σ spread associated with the E_n probability distribution for the given level of sample uncertainty. The mean E values are below the infinitely precise "model E" value. Black dot labeled III indicates mean of distribution of E_n values from Monte Carlo simulations for which sample uncertainties are very large, and grey band and error bars indicate 2σ probability distribution. The probability distribution of E values is significantly below the model exhumation rate.

settings the precise fault geometry and location at depth are not generally known a priori.

5.2. Probabilistic Model for the Influence of Sample Uncertainty on Exhumation Rate Interpretations

5.2.1. Effect of Sample Uncertainty on the Slope of the Best Fit Line Through Age-Elevation Data

[47] Up to this point we have focused on synthetic age distributions to explore the potential effects of topographic relief, exhumation rate and pathway on rate estimates derived from age-elevation gradients. While this exercise is necessary for gaining intuition regarding interactions of rock paths with the subsurface temperature field, ultimately we should ask how age-elevation gradients from natural samples vary as a function of sample uncertainty if we want to predict when the 1-D assumptions will significantly compromise our rate interpretations.

[48] It may appear logical to compare the percent error in the exhumation rate estimates predicted from the model to the percent sample uncertainty that characterizes a thermochronologic data set to evaluate whether or not the apparent exhumation rate it defines can be considered accurate. However, this exercise requires something more complicated than a simple comparison. This is because the larger the sample uncertainty, the higher the probability that the calculated age-elevation gradient will be different from the age-elevation gradient that would be defined by infinitely precise and accurate data. Because each apparent exhumation rate and its associated uncertainty are calculated directly from the slope of the best fit line through an array of age-elevation data, neither the apparent rate nor its associated uncertainty varies linearly with sample uncertainty. Sample uncertainties influence not only the error bars associated with the best fit slope, but the best fit slope itself.

[49] Consider three (x, y) points with the coordinates (1,1), (2,2), and (3,3). If the position of these points is known with infinite precision, the slope of the best fit line though these points is 1. However, uncertainties are associated with real data such that the actual measured values for three collinear points are likely not to be collinear. In all but the case for which the centroid value of each reported coordinate measurement happens to be perfectly accurate (e.g., (1.0 ± 0.1,1.0 ± 0.2), (2.0 ± 0.3,2.0 ± 0.1), (3.0 ± 0.1,3.0 ± 0.2)), a linear regression of such measurements would yield a value different from 1, although this slope might be statistically indistinguishable from 1 if the errors were suitably propagated. The error-induced variability in regression results can be simulated using a Monte Carlo technique. Assume that, for each of the (x, y) points, the measured y value actually varies from the nominal y value in a way described by a normal distribution of 5000 values with a 1% standard deviation. If we select a y value at random out of this distribution for each x, perform a linear regression on the new (x, y) points, and then repeat this exercise 10,000 times, we find that the resulting slope is 1.00 only about 47% of the time. If the uncertainty on each y value is increased to 50% and we repeat the regression another 10,000 times, the best fit slope is 1.00 only about 10% of the time. As the uncertainty on y increases, the number of times the "correct" slope is calculated falls, or the probability of getting an overestimate or underestimate rises. Because the best fit slope of an array of uncorrelated points is zero, the expected value of the best fit slope approaches zero as the sample uncertainty rises. As a result, the problem is compounded at large uncertainties and steeper slopes (i.e., slopes that are farther from zero).

5.2.2. Influence of Sample Uncertainty on Interpretation of Model Results

[50] In order to investigate the influence of this phenomenon on geologic interpretations, we explored the dependence of the best fit slope through an array of age-elevation data on sample uncertainties using a Monte Carlo approach. We created a distribution of 5000 normally distributed error

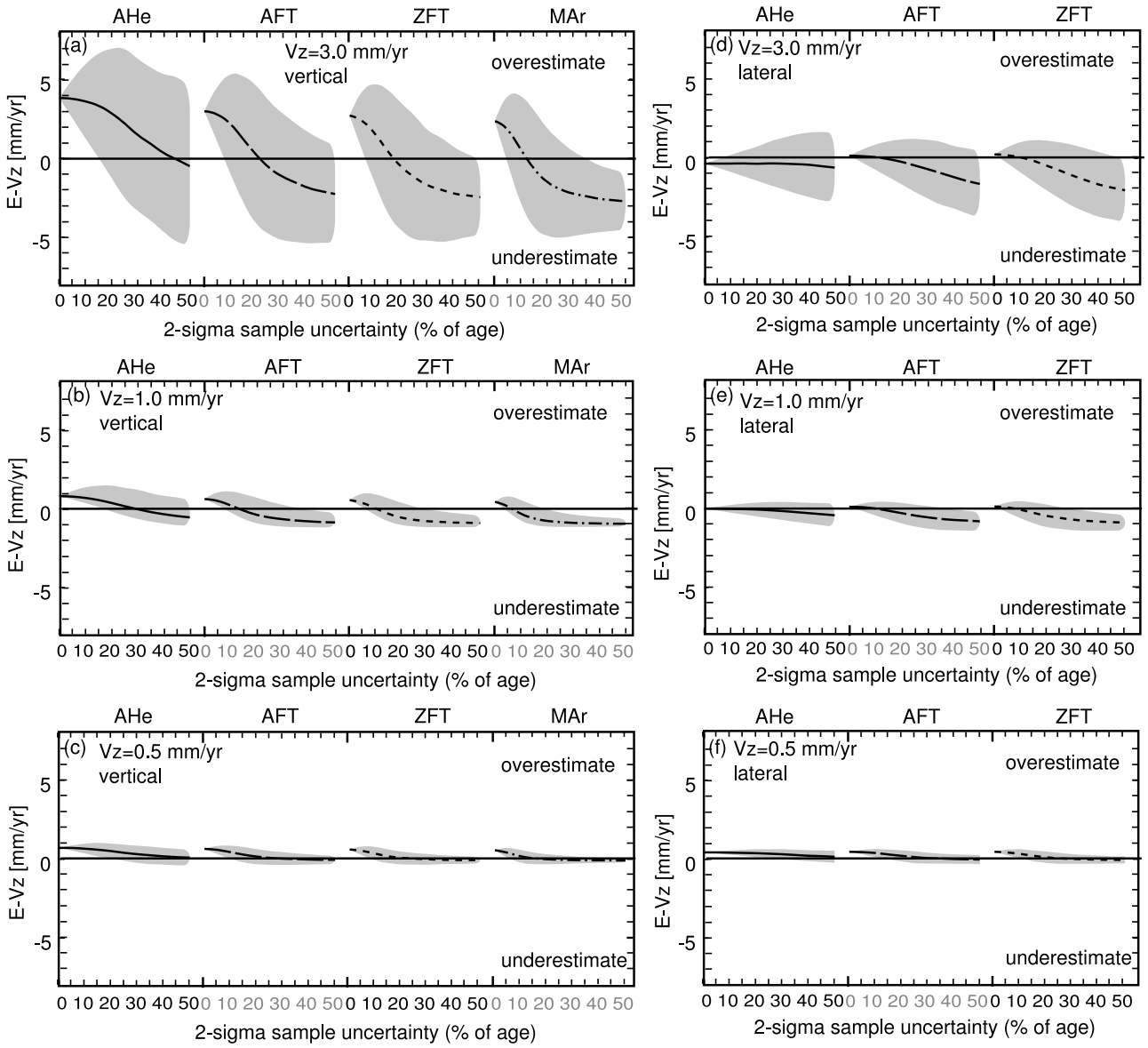

Figure 12. Difference between apparent and model exhumation rates ($E - v_z$) for profile A_{yz} as a function of sample uncertainty. Horizontal black lines at ($E - v_z$) = 0 mm/yr indicate the model exhumation rate. Black curves indicate values for AHe, long dashed curves indicate values for AFT, short dashed curves indicate values for ZFT, and dash-dotted curves indicate values for MAr. Grey shaded regions indicate 2σ range of age-elevation gradients. See section 5.2 and Figure 11.

values, ε, with a mean of zero and a 2σ standard deviation that is equal to the sample uncertainty U (%) to be associated with each age determination. For each predicted age a_i in a sample profile, a value ε_j was chosen randomly from the distribution of error values to be associated with a_i, such that $a_i' = a_i\ (\varepsilon_j + 1)$. The a_i' values for the sample profile were regressed to determine the apparent exhumation rate, E. This process was repeated n = 10,000 times for each sample profile to produce an array of E_n values. The mean and standard deviation of this distribution of E_n values characterize the probability distribution of expected age-elevation gradients for that sample profile as a function of sample uncertainty.

[51] If the age determinations are infinitely precise like our "zero uncertainty" model predicted ages, the apparent exhumation rate is given by the slope of the best fit age-elevation line, and the probability distribution of apparent rates is also infinitely small. In the cartoon shown in Figure 11, the age-elevation gradient at infinite precision overestimates the exhumation rate. If the sample uncertainty is moderate, the most likely slope of the best fit line through the age-elevation data decreases, and the range of expected slopes

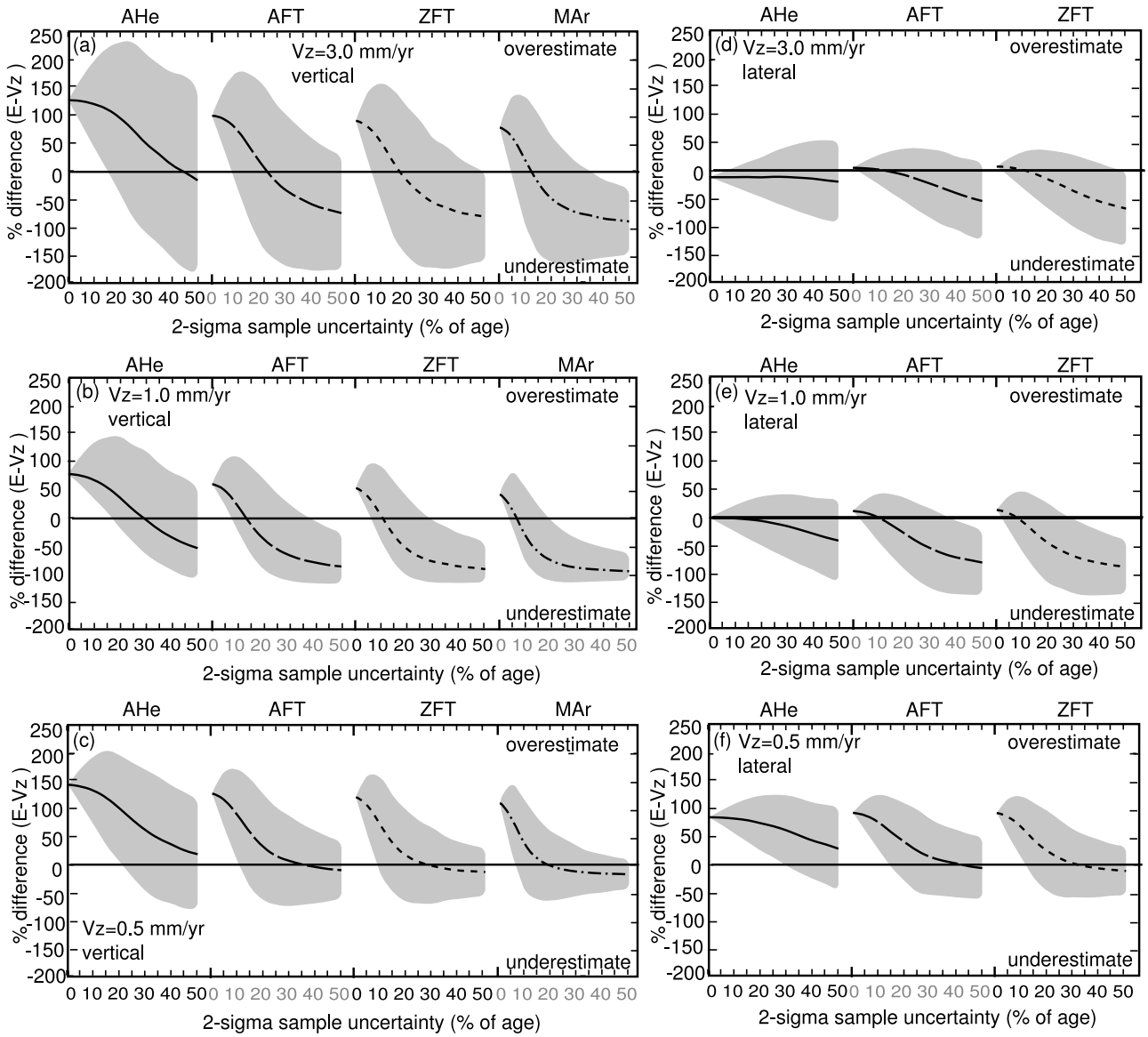

Figure 13. Percent difference between apparent and model exhumation rate [100*(E − v_z)/v_z] for profile A_{yz} as a function of sample uncertainty. Horizontal black lines at % difference (E − v_z) = 0 indicate true exhumation rate. Notation is as in Figure 12.

increases such that a proportion of the age-elevation gradients agree with the model exhumation rate (between points I and II). However, as the age determinations become much less precise, age and elevation become less well correlated, and the likelihood that the regression will return a slope of zero increases (point III). In the limit of infinitely large sample uncertainties, age and elevation are not expected to correlate at all, and the expected value of the best fit slope would always be zero. As a result, when sample uncertainty is very high, age-elevation gradients may underestimate the true rate by a large amount when exhumation is rapid but not when the exhumation rate is near zero. This effect causes the "curvature" in the grey (96% probability) region shown in Figure 11 because in this cartoon the apparent exhumation rate at infinite precision is shown to be greater than zero.

[52] The analysis shown schematically in Figure 11 was performed for a subset of the model age predictions (Figures 12 and 13). A profile oriented parallel to the direction of long-wavelength topography and lateral transport (in the YZ plane) was selected as an example because of the sensitivity of such profiles to different exhumation pathways. In particular, the profile at location A (Figure 2e), collected over a topographic slope of only 10°, was selected because it exhibited the largest exhumation rate errors we observed and thus provides a worst-case scenario example. These simulations indicate that exhumation rate estimates from age-elevation gradients vary not only as a function of

topography, exhumation rate and pathway, but also as a function of sample uncertainties (Figures 12 and 13).

[53] The pattern of best fit age-elevation gradients shown for a range of model exhumation rates in Figure 12 suggests that the magnitude of error in rate estimates should be greatest for highly precise, low-temperature thermochronometer data collected in rapidly eroding areas that are exhumed vertically. While the AHe age-elevation gradient for the vertical exhumation case shown in Figure 12a overestimates the model exhumation rate (v_z = 3.0 mm/yr) when sample uncertainty is relatively low (uncertainties less than ~15% of the measured date), it is likely to be within error of the exhumation rate when the data are less precise. In the analogous lateral exhumation case, the AHe thermochronometer is likely to very slightly underestimate the exhumation rate when the data are extremely precise, but otherwise provides an estimate that has a high probability of being within error of the exhumation rate (Figure 12d).

[54] In Figures 12a and 12d, the probability that age-elevation gradients for higher-temperature thermochronometer systems will be within error of the exhumation rate begins to rise at lower sample uncertainties than it does for the AHe age-elevation gradients. However, because the predicted ages (U = 0%) for higher-temperature thermochronometers overestimate the exhumation rate by a smaller amount, the probability that higher-temperature thermochronometers will begin to significantly underestimate the exhumation rate begins to increase at lower sample uncertainties than it does for the AHe thermochronometer. When the true exhumation rate is closer to zero, the expected magnitude of error in exhumation rate estimates from age-elevation gradients decreases and the range of probable apparent rates collapses (Figures 12b, 12c, 12e, and 12f). While the expected magnitude of error decreases for slower exhumation rates (Figure 12), the expected percent error increases when exhumation is gradual ($v_z \leq$ ~0.5–1.0 mm/yr, Figure 13f) [e.g., *Ehlers and Farley*, 2003].

5.2.3. Application of Model Results and Uncertainty Analysis to Natural Examples

[55] A relevant question is how can the model results and uncertainty analysis be applied to interpret real thermochronometer data? The probability curves described in the previous section for a "worst-case scenario" example can be used to evaluate the confidence we should have in the information we obtain from age-elevation gradients. The percent error in exhumation rate estimates can be large for vertically exhumed samples with AHe sample uncertainties below ~20%, and for higher-temperature system sample uncertainties of less than ~10–15% (Figures 13a–13c). The same is true when rocks are exhumed laterally, but only at slower rates (Figures 13d–13f). However, in terms of the magnitude of error, the results shown in Figure 12 suggest that even for a profile collected on a shallow, 10° slope in an orientation that is strongly influenced by long-wavelength topography and lateral advection, age-elevation gradients are likely to provide apparent rates within a mm/yr or so of the true rate given typical sample uncertainties. This is true for areas that erode at moderate to slow rates like the 1.0 and 0.5 mm/yr examples shown in Figure 12, with little sensitivity to sample uncertainty or exhumation pathway.

[56] In contrast, the magnitude of error for more rapidly eroding areas with high topographic relief is problematic for samples collected in such a profile (e.g., Figures 12a–12b), especially for the AHe thermochronometer. While 2σ uncertainties in thermochronometer ages for older samples can be much smaller [e.g., *Fitzgerald et al.*, 2006], typical 2σ uncertainties for AHe, AFT, ZFT, and MAr samples collected in a rapidly eroding landscape might be on the order of 5, 75, 20, and 5% of the measured date, respectively [e.g., *Huntington and Hodges*, 2006; *Blythe et al.*, 2007]. If this is the case and samples follow vertical exhumation pathways to the surface, the probability distributions in Figure 12a suggest that AHe and MAr age-elevation gradients would be likely to overestimate the exhumation rate while AFT samples underestimate it and ZFT age-elevation gradients are within error of it. If samples follow lateral exhumation pathways to the surface, AHe and ZFT age-elevation gradients would be likely to provide good exhumation rate estimates, while AFT samples might still underestimate the exhumation rate (Figure 12b). Even in this worst-case scenario, because sample uncertainty affects the error bars associated with rate estimates as well as these probability curves, in many cases the overestimates and underestimates are likely to be indistinguishable from the exhumation rate if uncertainties are propagated appropriately in the regression analysis.

[57] Significant errors in rate interpretations can still result, particularly when the data are precise and rocks are exhumed vertically. However, it is difficult to predict when significant errors will occur because the exhumation kinematics are not often known a priori. Figure 12 suggests that for an apparent AHe rate of 2.0 mm/yr with sample uncertainties of ~20–30%, if independent constraints on the exhumation pathway are unavailable, it would not be possible to distinguish among the exhumation pathways and exhumation rates shown in panels a, b, and d.

[58] A more encouraging observation is that, if sample uncertainty is sufficiently small, comparisons of multithermochronometer age-elevation gradients collected in a variety of profile orientations may provide detailed information regarding the subsurface kinematic and thermal fields. For example, our model results indicate that if age determinations are accurate and very precise (2σ uncertainties better than ~20% of the measured date for AHe, ~10–15% for AFT, and ~0–5% for the higher-temperature systems) and exhumation is sufficiently rapid (greater than ~0.5 mm/yr), age-elevation gradients for AHe, AFT, ZFT, and MAr thermochronometers should be in agreement if lateral transport is significant, and should vary systematically as a function of closure temperature if exhumation is vertical.

[59] Although our results indicate that age-elevation gradients are likely to provide reasonable exhumation rate estimates in many cases, in order to address some geologic questions it is more important to identify a change in exhumation rate than the rate itself. If the exhumation trajectory does not change significantly, can a simple one-dimensional interpretation of age-elevation gradients be

used to identify a rate change? On the basis of a difference in age-elevation gradients for AFT and MAr samples, *Huntington et al.* [2006] hypothesized that an abrupt exhumation rate acceleration occurred in the central Nepal Himalaya between ~2.5 and 0.9 Ma and used the same 3-D modeling approach described in this paper to confirm that their interpretation was robust. Our results suggest that their rate change interpretation is highly likely to be conservative. AFT dates from the Marsyandi valley, ranging in age from ~0.5 to 0.9 Ma, define an age-elevation gradient of 3.1 mm/yr [*Huntington et al.*, 2006], while MAr dates for the same samples define an age-elevation gradient of 0.57 mm/yr from 2.5 to 5.1 Ma [*Huntington and Hodges*, 2006]. The MAr data are relatively precise (5% average 2σ sample uncertainty), and from the results presented in Figures 12 and 13 we might expect the MAr age-elevation gradient to slightly overestimate the exhumation rate. Since the AFT data are much less precise (75% average 2σ sample uncertainty), we might actually expect the AFT age-elevation gradient to underestimate the exhumation rate when sample uncertainties are taken into account in this way. This suggests that a rate change interpretation based on the simple one-dimensional exhumation model is robust and conservative for this particular data set.

6. Conclusions

[60] Increasingly complex 2-D and 3-D thermal models have been used successfully to gain insight into potential complications associated with the age-elevation method of estimating exhumation rates. Because of such studies, it is well known that topography, erosion, and lateral transport during exhumation have the potential to influence exhumation rate estimates from age-elevation gradients [e.g., *Stüwe et al.*, 1994; *Mancktelow and Grasemann*, 1997; *Batt and Brandon*, 2002]. Previous work has also alluded to the fact that sample profile orientation can affect apparent exhumation rates [*Braun*, 2002a], and our work indicates that apparent exhumation rates are indeed sensitive to the orientation of age-elevation profiles with respect to long-wavelength topographic features and the direction of transport.

[61] Given these potential complications, what is the likelihood that it is reasonable to use age-elevation data to investigate geologic questions of interest, and to what extent are sophisticated thermal models needed to interpret them? A simple 1-D exhumation model is associated with a correspondingly simple, short list of assumptions, and this is advantageous as long as the model adequately describes the physics of the problem. On the other end of the spectrum, sophisticated 3-D models account for the influence of processes that are ignored in 1-D models, but are associated with similarly sophisticated sets of assumptions. As it is impossible to test many of these assumptions, we would like to strike a balance where the most geologically meaningful information is obtained with the fewest assumptions regarding the interpretation of thermochronologic data.

[62] Like many previous workers [e.g., *Stüwe et al.*, 1994], we compared a 1-D interpretation of synthetic age-elevation gradients to the exhumation rate prescribed in the multidimensional model that produced them; however, the error in apparent exhumation rates from synthetic data does not directly translate to the error that would be observed for real data when sample uncertainties are considered. Sample uncertainties change the probability that a regression through the data will return the same age-elevation gradient that would be calculated if the cooling ages were infinitely precise and accurate. The relationship between this probability and sample uncertainty varies nonlinearly, and the effect is most pronounced for rapid apparent exhumation rates and imprecise data. Highly precise, low-temperature thermochronometer data collected in rapidly eroding areas are unlikely to provide robust exhumation rate estimates that are within uncertainty of the true rate even when the influence of sample uncertainty on the age-elevation gradient is considered. However, because sample uncertainties also affect error bars associated with rate estimates, the age-elevation approach can provide exhumation rate estimates that are within uncertainty of the true rate even for profiles collected under unfavorable conditions. Given typical thermochronometer uncertainties, age-elevation gradients can be interpreted in a straightforward way to yield geologically meaningful information regarding exhumation rates and rate changes, especially if samples are collected along moderately steep topographic slopes.

[63] However, the influence of topography, exhumation rate and pathway on synthetic age distributions from sophisticated thermal models *is* significant in some cases. This suggests that if age determinations are sufficiently precise and accurate, the results of age-elevation gradients for different sample profile orientations and a range of thermochronometers might be used to reconstruct both rock trajectories and exhumation rates in complicated tectonic settings. While our model results are nonunique, and similar age distributions may be produced with different combinations of parameters, our results suggest that a combination of 3-D thermal modeling, creative sample collection strategies, and highly precise and accurate analyses of multiple thermochronometers can be used in a straightforward way to constrain rock exhumation pathways in active orogens.

Appendix A

[64] We use thermal model simulations for simplified exhumation geometries to predict cooling-rate-dependent cooling ages for a range of thermochronometers sampled on 3-D topography. *Whipp et al.* [2007] combined the same modeling approach with apatite fission track ages from central Nepal to investigate Quaternary Himalayan exhumation. This modeling approach combines a kinematic model, thermal finite element model, and thermochronometer age prediction model, as described below.

A1. Kinematic Model

[65] The kinematic model we used explores three exhumation geometries we refer to as "vertical" (Figure 2a), "lateral" (Figure 2b), and "thrust" (Figure 2c). Mass is conserved in the model, and the material is assumed to be

incompressible. For the purposes of this study, we also assume that topography is static, such that the vertical erosional exhumation rate at the surface is the same as the vertical component of velocity in the kinematic model, v_z, (ranging from 0.1 to 3.0 mm/yr for the synthetic sample locations). Note that the velocity v_z defines the vertical component of the model exhumation rate (referred to as simply the "model exhumation rate") to be compared to the apparent exhumation rate, E, derived from the age-elevation gradient given by predicted ages in the model. Table 2 summarizes the rates and geometries explored in each of the model simulations we highlight in this paper. Rocks in each of these geometries do not move with respect to the X direction during exhumation, but predicted cooling ages are affected in the X direction due to the influence of 3-D topography on the thermal field.

[66] While the Y position of each rock also remains fixed in the vertical models, material is transported in the Y direction in the lateral and thrust models. In the lateral models, the velocity v_y is a function of the prescribed exhumation rate v_z and the dip of the rock trajectory (held constant in all lateral simulations at 28°):

$$v_y = \left| \frac{v_z}{\tan(28^\circ)} \right| \tag{A1}$$

We note that in this formulation the Y coordinate does not correspond to geographic North; although we used the same topography used by *Whipp et al.* [2007], the coordinate system is rotated with respect to geographic coordinates such that the Y axis is parallel to the shortening direction across the Main Central Thrust (MCT). The assumed shortening direction (198°) is subparallel to the transport direction inferred from measured stretching lineations in the MCT shear zone [*Brunel*, 1986], and is consistent with the present-day convergence direction between the Tibetan Plateau and India as measured by GPS [*Bilham et al.*, 1997; *Larson et al.*, 1999; *Wang et al.*, 2001; *Jouanne et al.*, 2004; *Zhang et al.*, 2004]. A trajectory dip of 28° was chosen to approximate the dip of the MCT beneath the study area [e.g., *Lavé and Avouac*, 2000]. In the thrust models, faults are approximated as planar surfaces composed of two segments, as shown in Figure 2c, and slip occurs parallel to the model fault planes. The dip angle Θ is 0° for the horizontal segment at 28 km depth and 28° for the ramp segment of the fault. The rate of underthrusting is set to equal half of the total lateral convergence velocity across the fault, v_{converge}. The velocity v_{converge} is set to yield vertical exhumation rates of interest for comparison to the vertical and lateral models in the hanging wall of the thrust. The slip rate on the fault is a function of the dip angle of the structure and v_{converge}, and was calculated as follows:

$$v_{\text{slip}} = \frac{|v_{\text{converge}}|}{\cos\theta_i} \tag{A2}$$

where Θ_i is the ith dip plane of the fault. The range of convergence rates explored in the thrust simulations is 0.19–5.6 mm/yr (corresponding to v_z = 0.1–3.0 mm/yr in the immediate hanging wall of the thrust, Table 2). For the thrust models, we only predict ages for samples located in the hanging wall of the fault. v_y for these rocks is equal to $v_{\text{converge}}/2$, and their vertical exhumation rate v_z(x, y, z) is given by

$$v_z(x,y,z) = v_y \tan\theta_i \tag{A3}$$

A2. Thermal Model

[67] We calculated the 3-D thermal field of a 140 × 84 km region of mountainous topography to 50 km depth [see *Whipp et al.*, 2007]. The subsurface thermal field is calculated using the steady state advection-diffusion equation

$$\frac{\nabla(K\nabla T)}{\rho c} - \bar{v}\nabla T = -\frac{A}{\rho c} \tag{A4}$$

where T is temperature and $\bar{v}$ is the material velocity from the kinematic model. K, A, ρ, and c are the thermal conductivity, radiogenic heat production per unit volume, density, and heat capacity, respectively. The finite element program FRACTure [*Kohl and Hopkirk*, 1995; *Kohl et al.*, 2001] is used to solve equation (A4) in the Eulerian (spatial) reference frame.

[68] In order to avoid boundary effects, the thermal model extends an average of 20 km from the edges of the box containing the synthetic "sample" locations shown in Figure 2e. The upper surface has a constant temperature boundary condition, and temperatures are fixed at 14°C at sea level and decrease at an atmospheric lapse rate of 7°C per kilometer of elevation increase. Values for the constant temperature boundary condition at the base of the model and material properties investigated are summarized in Table 1. Velocity-dependent shear heating is included to account for frictional heating on the fault planes after the method of *Henry et al.* [1997]. Like *Whipp et al.* [2007], we follow the moderate friction case of *Hansen and Carter* [1982], where the fault zone is assumed to be 1 km wide and the strain rate is equal to the slip rate across the fault. The maximum allowed shear stress is 50 MPa. It is calculated using a brittle pressure-dependent law or ductile temperature-dependent power law, whichever produces the smaller result. The additional heat produced is added to the nodal radiogenic heat production within the shear zone, and it is assumed that heat transfer by fluid flow is not a major thermal influence.

A3. Thermochronometer Age Prediction

[69] Thermochronometer ages for apatite (U-Th)/He (AHe), apatite fission track (AFT), zircon fission track (ZFT), and muscovite $^{40}Ar/^{39}Ar$ (MAr) samples were calculated using model-predicted cooling histories for rocks coincident with the 72 sample locations shown in Figure 2e. Cooling histories were calculated by tracking samples from the surface back to different depths in the model. Predicted fission track ages were calculated for apatite and zircon

using the method outlined by *Ehlers et al.* [2005], and predicted AHe ages were calculated according to the method used by *Ehlers and Farley* [2003]. MAr ages were calculated using a nominal closure temperature of 350°C.

Notation

E age-elevation gradient, or apparent erosional exhumation rate.
v_z vertical velocity vector in kinematic model, equals model exhumation rate.
X, Y, Z coordinate axes (see Figures 2a–2c).
T_C closure temperature.
x_1 thermochronologic sample x_1.
t_{x1} cooling age for sample x_1.
z_{x1} elevation of sample x_1.
AHe apatite (U-Th)/He.
AFT apatite fission track.
ZFT zircon fission track.
MAr muscovite $^{40}Ar/^{39}Ar$.
U 2σ characteristic sample% uncertainty (see section 5.2).
ε distribution of 5000 normally distributed error values with a mean of zero and a 2σ standard deviation that is equal to U.

[70] **Acknowledgments.** We would like to thank Kelin Whipple, David Mohrig, and Stephane Rondenay for stimulating discussions regarding this work and for constructive comments on a previous version of the manuscript. The paper benefited from thoughtful reviews by Lothar Ratschbacher and two anonymous readers. This work is a product of the NSF Continental Dynamics project "Geomorphic-Geodynamic Coupling at the Orogen Scale."

References

Balestrieri, M. L., M. Bernet, M. T. Brandon, V. Picotti, P. Reiners, and M. Zattin (2003), Pliocene and Pleistocene exhumation and uplift of two key areas of the Northern Apennines, *Quat. Int.*, *101–102*, 67–73.

Bartolini, C. D., N. Agostino, and F. Dramis (2003), Topography, exhumation, and drainage network evolution of the Apennines, *Episodes*, *26*, 212–216.

Batt, G., and M. T. Brandon (2002), Lateral thinking: 2D interpretation of thermochronology in convergent orogenic settings, *Tectonophysics*, *349*, 185–201.

Batt, G. E., and J. Braun (1997), On the thermomechanical evolution of compressional orogens, *Geophys. J. Int.*, *128*, 364–382.

Batt, G., and J. Braun (1999), The tectonic evolution of the Southern Alps, New Zealand: Insights from fully thermal coupled dynamical modelling, *Geophys. J. Int.*, *136*, 403–420.

Batt, G. E., M. T. Brandon, K. A. Farley, and M. Roden-Tice (2001), Tectonic synthesis of the Olympic Mountains segment of the Cascadia wedge, using two-dimensional thermal and kinematic modeling of thermochronological ages, *J. Geophys. Res.*, *106*, 26,731–26,746.

Bilham, R., K. Larson, and J. Freymueller (1997), GPS measurements of present-day convergence across the Nepal Himalaya, *Nature*, *386*, 61–64.

Bird, P., M. N. Toksöz, and N. H. Sleep (1975), Thermal and mechanical models of continent-continent collision zones, *J. Geophys. Res.*, *80*, 4405–4416.

Blythe, A. E., D. W. Burbank, A. Carter, K. Schmidt, and J. Putkonen (2007), Plio-Quaternary exhumation history of the central Nepalese Himalaya: 1. Apatite and zircon fission track and apatite [U-Th]/He analyses, *Tectonics*, *26*, TC3002, doi:10.1029/2006TC001990.

Bollinger, L., J. P. Avouac, O. Beyssac, E. J. Catlos, T. M. Harrison, M. Grove, B. Goffé, and S. Sapkota (2004), Thermal structure and exhumation history of the Lesser Himalaya in central Nepal, *Tectonics*, *23*, TC5015, doi:10.1029/2003TC001564.

Bollinger, L., P. Henry, and J. P. Avouac (2006), Mountain building in the Nepal Himalaya: Thermal and kinematic model, *Earth Planet. Sci. Lett.*, *244*, 58–71.

Brandon, M. T., M. K. Roden-Tice, and J. I. Garver (1998), Late Cenozoic exhumation of the Cascadia accretionary wedge in the Olympic Mountains, northwest Washington State, *Geol. Soc. Am. Bull.*, *110*, 985–1009.

Braun, J. (2002a), Estimating exhumation rate and relief evolution by spectral analysis of age-elevation datasets, *Terra Nova*, *14*, 210–214.

Braun, J. (2002b), Quantifying the effect of recent relief changes on age-elevation relationships, *Earth Planet. Sci. Lett.*, *200*, 331–343.

Braun, J. (2005), Quantitative constraints on the rate of landform evolution derived from low-temperature thermochronology, in *Low-Temperature Thermochronology: Techniques, Interpretations, and Applications*, *Rev. Mineral. Geochem.*, vol. 58, edited by P. W. Reiners and T. A. Ehlers, pp. 351–374, Mineral. Soc. of Am., Washington, D. C.

Brewer, I. D., D. W. Burbank, and K. V. Hodges (2003), Modelling detrital cooling-age populations: insights from two Himalayan catchments, *Basin Res.*, *15*, 305–320.

Brewer, I. D., D. W. Burbank, and K. V. Hodges (2006), Downstream development of a detrital cooling-age signal: Insights from $^{40}Ar/^{39}Ar$ muscovite thermochronology in the Nepalese Himalaya, in *Tectonics, Climate, and Landscape Evolution*, edited by S. D. Willett et al., *Spec. Pap. Geol. Soc. Am.*, *398*, 321–338.

Brunel, M. (1986), Ductile thrusting in the Himalayas: Shear sense criteria and stretching lineations, *Tectonics*, *5*, 247–265.

Burbank, D. W., A. E. Blythe, J. Putkonen, B. Pratt-Sitaula, E. Gabet, M. Oskin, A. Barros, and T. P. Ojha (2003), Decoupling of erosion and precipitation in the Himalaya, *Nature*, *426*, 652–655.

Cattin, R., and J. P. Avouac (2000), Modeling mountain building and the seismic cycle in the Himalaya of Nepal, *J. Geophys. Res.*, *105*, 13,389–13,408.

Crowley, P. D., P. W. Reiners, J. M. Reuter, and G. D. Kaye (2002), Laramide exhumation of the Bighorn Mountains, Wyoming: An apatite (U-Th)/He thermochronology study, *Geology*, *30*, 27–30.

Ducea, M., M. A. House, and S. Kidder (2003), Late Cenozoic denudation and uplift rates in the Santa Lucia Mountains, California, *Geology*, *31*, 139–142.

Edwards, R. M. (1995), $^{40}Ar/^{39}Ar$ geochronology of the Main Central thrust (MCT) region: Evidence for late Miocene to Pliocene disturbances along the MCT, Marsyangdi River valley, west-central Nepal Himalaya, *J. Nepal Geol. Soc.*, *10*, 41–46.

Ehlers, T. A. (2005), Crustal thermal processes and the interpretation of thermochronometer data, in *Low-Temperature Thermochronology: Techniques, Interpretations, and Applications*, *Rev. Mineral. Geochem.*, vol. 58, edited by P. W. Reiners and T. A. Ehlers, pp. 315–350, Mineral. Soc. of Am., Washington, D. C.

Ehlers, T. A., and K. A. Farley (2003), Apatite (U-Th)/He thermochronometry: methods and applications to problems in tectonic and surface processes, *Earth Planet. Sci. Lett.*, *206*, 1–14.

Ehlers, T. A., P. A. Armstrong, and D. S. Chapman (2001), Normal fault thermal regimes and the interpretation of low-temperature thermochronometers, *Phys. Earth Planet. Inter.*, *126*, 179–194.

Ehlers, T. A., T. Chaudhri, and S. Kumar (2005), Computational tools for low-temperature thermochronometer interpretation, in *Low-Temperature Thermochronology: Techniques, Interpretations, and Applications*, *Rev. Mineral. Geochem.*, vol. 58, edited by P. W. Reiners and T. A. Ehlers, pp. 589–622, Mineral. Soc. of Am., Washington, D. C.

Fitzgerald, P. G., S. L. Baldwin, L. E. Webb, and P. B. O'Sullivan (2006), Interpretation of (U–Th)/He single grain ages from slowly cooled crustal terranes: A case study from the Transantarctic Mountains of southern Victoria Land, *Chem. Geol.*, *225*(1–2), 91–120, doi:10.1016/j.chemgeo. 2005.09.001.

Foster, D. A., and A. J. W. Gleadow (1996), Structural framework and denudation history of the flanks of the Kenya and Anza rifts, East Africa, *Tectonics*, *15*, 258–271.

Gleadow, A. J. W., and I. R. Duddy (1981), A natural long-term track annealing experiment for apatite, *Nuclear Tracks*, *5*, 169–174.

Hansen, F. D., and N. L. Carter (1982), Creep of selected crustal rocks at 1000 MPa, *Eos Trans. AGU*, *63*, 437.

Henry, P., X. Le Pichon, and B. Goffé (1997), Kinematic, thermal and petrological model of the Himalayas: constraints related to metamorphism within the underthrust Indian crust and topographic elevation, *Tectonophysics*, *273*, 31–56.

Hodges, K., C. Wobus, K. Ruhl, T. Schildgen, and K. Whipple (2004), Quaternary deformation, river steepening, and heavy precipitation at the front of the Higher Himalayan ranges, *Earth Planet. Sci. Lett.*, *220*, 379–389.

Hodges, K. V. (2003), Geochronology and thermochronology in orogenic systems, in *The Crust*, edited by R. L. Rudnick, pp. 263–292, Elsevier Sci., Amsterdam.

House, M. A., S. A. Kelley, and M. Roy (2003), Refining the footwall cooling history of a rift flank uplift, Rio Grande Rift, New Mexico, *Tectonics*, *22*(5), 1060, doi:10.1029/2002TC001418.

Huntington, K. W., and K. V. Hodges (2006), A comparative study of detrital mineral and bedrock age-elevation methods for estimating erosion rates, *J. Geophys. Res.*, *111*, F03011, doi:10.1029/2005JF000454.

Huntington, K. W., A. E. Blythe, and K. V. Hodges (2006), Climate change and late Pliocene acceleration of erosion in the Himalaya, *Earth Planet. Sci. Lett.*, *252*, 107–118.

Jouanne, F., J. L. Mugnier, J. F. Gamond, P. L. Fort, M. R.Pandey, L. Bollinger, M. Flouzat, and J. P.

Avouac (2004), Current shortening across the Himalayas of Nepal, *Geophys. J. Int.*, *157*, 1–14.

Kohl, T. (1999), Transient thermal effects below complex topographies, *Tectonophysics*, *306*, 311–324.

Kohl, T., and R. J. Hopkirk (1995), "FRACTure" a simulation code for forced fluid flow and transport in fractured porous rock, *Geothermics*, *24*(3), 345–359.

Kohl, T., S. Signorelli, and L. Rybach (2001), Three-dimensional (3-D) thermal investigation below high Alpine topography, *Phys. Earth Planet. Inter.*, *126*, 195–210.

Larson, K., et al. (1999), Kinematics of the India-Eurasia collision zone from GPS measurements, *J. Geophys. Res.*, *104*, 1077–1093.

Lavé, J., and J. P. Avouac (2000), Active folding of fluvial terraces across the Siwalik Hills, Himalayas of central Nepal, *J. Geophys. Res.*, *105*, 5735–5770.

Mancktelow, N. S., and B. Grasemann (1997), Time-dependent effects of heat advection and topography on cooling histories during erosion, *Tectonophysics*, *270*, 167–195.

Oxburgh, E. R., and D. L. Turcotte (1974), Thermal gradients and regional metamorphism in overthrust terrains with special reference to the eastern Alps, *Schweiz. Mineral. Petrogr. Mitt.*, *54*, 641–642.

Pandey, M. R., R. P. Tandukar, J. P. Avouac, J. Lavé, and J. P. Massot (1995), Interseismic strain accumulation on the Himalayan Crustal Ramp (Nepal), *Geophys. Res. Lett.*, *22*, 751–754.

Reiners, P. W., T. A. Ehlers, J. I. Garver, S. Gran Mitchell, D. R. Montgomery, J. A. Vance, and S. Nicolescu (2002), Late Miocene exhumation and uplift of the Washington Cascade Range, *Geology*, *30*, 767–770.

Reiners, P. W., T. A. Ehlers, S. G. Mitchell, and D. R. Montgomery (2003), Coupled spatial variations in precipitation and long-term erosion rates across the Washington Cascades, *Nature*, *426*, 645–647.

Ruhl, K. W., and K. V. Hodges (2005), The use of detrital mineral cooling ages to evaluate steady state assumptions in active orogens: An example from the central Nepalese Himalaya, *Tectonics*, *24*, TC4015, doi:10.1029/2004TC001712.

Ruppel, C., and K. V. Hodges (1994), Role of horizontal thermal conduction and finite time thrust emplacement in simulation of pressure-temperature-time paths, *Earth Planet. Sci. Lett.*, *123*, 49–60.

Safran, E. B. (2003), Geomorphic interpretation of low-temperature thermochronologic data: Insights from two-dimensional thermal modeling, *J. Geophys. Res.*, *108*(B4), 2189, doi:10.1029/2002JB001870.

Seeber, L., and V. Gornitz (1983), River profiles along the Himalayan arc as indicators of active tectonics, *Tectonophysics*, *92*, 335–367.

Stockli, D. F., K. A. Farley, and T. A. Dumitru (2000), Calibration of the apatite (U-Th)/He thermochronometer on an exhumed fault block, White Mountains, California, *Geology*, *28*, 983–986.

Stüwe, K., and M. Hintermüller (2000), Topography and isotherms revisited: the influence of laterally migrating drainage divides, *Earth Planet. Sci. Lett.*, *184*, 287–303.

Stüwe, K., L. White, and R. Brown (1994), The influence of eroding topography on steady-state isotherms: Application to fission track analysis, *Earth Planet. Sci. Lett.*, *124*, 63–74.

Thiede, R. C., et al. (2004), Climatic control on rapid exhumation along the southern Himalayan front, *Earth Planet. Sci. Lett.*, *222*, 791–806.

Toksoz, M. N., and P. Bird (1977), Modeling of temperatures in continental convergence zones, *Tectonophysics*, *41*, 181–193.

van der Beek, P., and J. Braun (1999), Controls on post mid-Cretaceous landscape evolution in the southeastern highlands of Australia: Insights from numerical surface process models, *J. Geophys. Res.*, *104*, 4945–4966.

Wagner, G. A., and G. M. Reimer (1972), Fission track tectonics: The tectonic interpretation of fission track apatite ages, *Earth Planet. Sci. Lett.*, *14*, 263–268.

Wagner, G. A., G. M. Reimer, and E. Jaeger (1977), Cooling ages derived by apatite fission track, mica Rb-Sr, and K-Ar dating: The uplift and cooling history of the central Alps, *Mem. Ist. Geol. Min. Univ. Padova*, *30*, 1–27.

Wang, Q., et al. (2001), Present-day crustal deformation in China constrained by Global Positioning System measurements, *Science*, *294*, 574–577.

Whipp, D. M., and T. A. Ehlers (2007), Influence of groundwater flow on thermochronometer-derived exhumation rates in the central Nepalese Himalaya, *Geology*, in press.

Whipp, D. M. Jr., T. A. Ehlers, A. E. Blythe, K. W. Huntington, K. V. Hodges, and D. W. Burbank (2007), Plio-Quaternary exhumation history of the central Nepalese Himalaya: 2. Thermokinematic and thermochronometer age prediction model, *Tectonics*, *26*, TC3003, doi:10.1029/2006TC001991.

Wolf, R. A., K. A. Farley, and D. M. Kass (1998), Modeling of the temperature sensitivity of the apatite (U-Th)/He thermochronometer, *Chem. Geol.*, *148*(1–2), 105–114.

Zhang, P., et al. (2004), Continuous deformation of the Tibetan Plateau from Global Positioning System data, *Geology*, *32*, 809–812.

T. A. Ehlers and D. M. Whipp Jr., Department of Geological Sciences, University of Michigan, Ann Arbor, MI 48109, USA.

K. V. Hodges, School of Earth and Space Exploration, Arizona State University, Tempe, AZ 85287, USA.

K. W. Huntington, Division of Geological and Planetary Sciences, California Institute of Technology, Pasadena, CA 91125, USA. (kateh@gps.caltech.edu)